Master of Science Thesis
VT2019

Quantification of I-131 Activity from Gamma Camera Images of Thyroid Cancer Patients

Frida Westerbergh

Supervisors

Cecilia Hindorf, Erik Larsson och Anna Stenvall

Department of Medical Radiation Physics,
Clinical Sciences, Lund
Lund University
www.msf.lu.se

Popularized summary in Swedish

Att behandla sköldkörtelcancer med radioaktivt jod:

Hur mycket jod tas upp av en cancertumör?

Populärvetenskaplig sammanfattning

Jod är ett grundämne som är livsnödvändigt för människan. Det finns att hitta i bland annat fisk, skaldjur ägg och mejeriprodukter. Många av oss har även jodberikat salt på middagsbordet. En del av det jod vi får i oss via kosten kommer att ansamlas i sköldkörteln - ett organ som sitter under struphuvudet, på halsens nedre del. Sköldkörteln har i uppgift att producera hormoner. Dessa hormoner utsöndras i blodet, och tas upp av kroppens alla vävnader, där de hjälper cellerna att reglera sin ämnesomsättning. Sköldkörteln påverkar därmed många av kroppens viktiga funktioner. För att produktionen av sköldkörtelhormoner skall fungera normalt krävs jod.

Det jod som finns i vårt hushållssalt har en syster – det radioaktiva jodet. Kroppen ser ingen skillnad på dessa två. Om radioaktivt jod tillförs kroppen kommer detta omsättas på samma sätt som vanligt jod, men med en viktig skillnad – det strålar! Denna egenskap utnyttjar man för att behandla sjukdomar i sköldkörteln, däribland sköldkörtelcancer. Radioaktivt jod tas upp av cancercellerna, vilka därmed strålas sönder. Vidare kan man, genom att detektera strålningen i en så kallad gammakamera, avbilda jodets fördelning i kroppen, och på så sätt få en bild av sjukdomens utbredning.

Vid bildtagning med gammakameran genereras tvådimensionella bilder av det radioaktiva läkemedlet i patienten. Vidare kan man genom att låta kameran rotera runt patienten kan man även framkalla tredimensionella bilder – en metod som kallas Single Photon Emssion Computed Tomography (*SPECT*). Syftet med detta examensarbete är att, utifrån nuklearmedicinska bilder av patienter som genomgått terapi med radioaktivt jod, utveckla en metod för att bestämma mängden jod som tagits upp av en cancertumör. För att göra detta krävs vetskap om de processer som äger rum, från dess att strålningen skickas ut, till dess att den färdiga bilden har framställts. Vidare måste man ha metoder för att kompensera för den försämring i bildkvalité som vissa av dessa processer kan föra med sig. Detta arbete fokuserar på just detta; hur gör man för att kvantifiera mängden jod i en tumör, och hur skall man förhålla sig till de faktorer som försvårar beräkningarna?

Det långsiktiga målet med arbetet är att göra det möjligt att bestämma vilken stråldos en patient erhåller i samband med en cancerbehandling med radioaktivt jod, och därigenom potentiellt lägga grunden för en förbättrad framtida behandling.

Abstract

BACKGROUND: Radioiodine (^{131}I) has been used in thyroid cancer treatments for many years, and has demonstrated good results with regards to disease management. Radioiodine therapy is however partially empirical, as not very much is known concerning radiation dosimetry. At Skåne University Hospital, the number of treatments has been growing steadily over the past couple of years, resulting in an increased demand for dosimetry. The aim of this thesis was to develop a method for patient-specific ^{131}I activity quantifications, and thereby provide a foundation for patient-specific dosimetry at Skåne University Hospital.

METHOD: Planar measurements were performed to evaluate the degradation from penetration and scatter, and assess the effectiveness of two different window based scatter corrections (namely a DEW and a TEW correction). Calibration factors were established for planar and SPECT acquisitions, and the NEMA Body Phantom was used to study partial volume effects. Lastly, an anthropomorphic phantom study was carried through to test the quantification method and thereby assess potential quantification errors in patient imaging.

RESULTS: For spherical structures, quantifications errors of up to 40% were obtained for planar images, while SPECT quantification errors were generally below 10%. For non-spherical structures, the error was significantly increased. In the planar studies of scatter and penetration, a TEW scatter correction was shown to be most effective. However, in quantifications, the scatter correction appeared to have little impact on the accuracy of the results. Instead, the quantification error seem to majorly depend on size and shape of the lesion, as well as the overall attenuation properties of the examined object.

CONCLUSIONS: With the developed method, accurate SPECT quantifications are feasible. However, a varying patient geometry can potentially induce significant errors, as a window based scatter correction alone cannot compensate for large variations in the level of attenuation. Hence, the accuracy of the calibration is crucial. Object shape effects appear to be significant, as applying a sphere-based recovery coefficient to a non-spherical structure will not recover all of the activity, and errors remain large. Planar quantifications are generally associated with large errors, and accurate planar quantifications would be difficult to achieve in patient imaging.

Additional work is needed to improve the accuracy of the method. Non-spherical recovery coefficient needs to be established, and effects of variations in patient geometry and ^{131}I uptake should be examined more thoroughly. Furthermore, the reconstruction protocol should be optimized. In order for dosimetry to be performed, methods of mass determination would need to be explored. Also, methods of determining the effective half-life would need assessment.

Acknowledgements

I would like to express my deepest gratitude to my supervisors for the support they have offered over the course of this project;

To Cecilila Hindorf, for her valuable ideas, useful critique and guidance throughout the project.

To Erik Larsson, for his great dedication to the project and patience in guiding me through the data analysis.

To Anna Stenvall, for her constant encouragement and support.

Finally, I wish to thank Skåne University Hospital for generously allowing me use their equipment, as well as the extended staff for kindly welcoming me into the organization.

Abbreviations

AC	Attenuation Correction
ATA	American Thyroid Association
CDR	Collimator Detector Response
CT	Computed Tomography
DEW	Dual Energy Window
FOV	Field Of View
HEGP	High Energy General Purpose
IR	Iterative Reconstruction
MLEM	Maximum Likelihood Expectation Maximization
OSEM	Ordered Subset Expectation Maximization
PF	Penetration Factor
PMMA	Polymethyl Methacrylate
PVE	Partial Volume Effects
RC	Recovery Coefficient
ROI	Region Of Interest
RR	Resolution Recovery
SC	Scatter Correction
SUS	Skåne University Hospital
SPECT	Single Photon Emission Computed Tomography
TEW	Triple Energy Window
VOI	Volume Of Interest

Table of Contents

1 Introduction

1.1 Background

Thyroid cancers are considered rare. Out of the 60 000 new cases of cancer diagnosed in Sweden each year, thyroid cancers account for approximately 1%.[1,2] However, an increase in incidence has been observed over the past decade. In 2018, the Swedish Cancer Society reported an average yearly increase of 4.3% and 2.9% for women and men, respectively.[2] At Skåne University Hospital (*SUS*), the number of thyroid cancer treatments has increased accordingly.

Thyroid cancers are usually treated with a thyroidectomy – a surgical procedure in which the thyroid gland is removed, either partially or entirely. The procedure is commonly accompanied by an administration of radioactive iodine; ^{131}I. A small fraction of the administered iodine will accumulate in the remaining thyroid tissue. On decaying, ^{131}I will emit beta particles. These emissions will induce biological damage to nearby tissue, generating a therapeutic effect. Hence, residual disease can be treated. Furthermore, the ^{131}I decay will yield gamma emissions, which are used to image the distribution of the radiopharmaceutical.

After the ^{131}I administration, patients are hospitalized to minimize public radiation exposure. Patients are discharged when activity levels have sufficiently declined. Five to six days after the administration, patients return for a post therapeutic imaging session. The purpose of the session is to study the ^{131}I uptake, and thereby provide diagnostic information regarding the stage of the disease. The session begins with a planar whole-body scan. If the scan reveals any unusual uptake or new pathology, additional SPECT/CT imaging is performed to further study the lesion.

Currently, the ^{131}I images acquired at SUS are qualitatively analyzed, i.e. through visual evaluation. No activity quantifications or dosimetric calculations are routinely performed. However, with ^{131}I treatments growing in number, a further interest in dosimetry has arisen. The need for dosimetry is especially large for patients who receive additional external beam therapy for distant metastases, since the treatment planning requires dose assessments with respect to critical organs. Dosimetry could also be used for quantitative assessments of treatment response, and potentially in future optimizations of radioiodine treatments.

1.2 Aim

The aim of this project was to develop a method for gamma camera based ^{131}I activity quantifications for thyroid cancer patients treated at SUS, and thereby provide a foundation for patient-specific dosimetry.

[1] NORDCAN. Cancer Statistics Fact Sheet – The Thyroid Gland. Association of the Nordic Cancer Registries; 2019.
[2] Swedish Cancer Society. Cancerfondsrapporten 2018. Stockholm: Swedish Cancer Society; 2018.

2 Theory

2.1 Thyroid carcinoma: Background and current clinical practice

The thyroid is a large, endocrine gland located on the base of the neck. It consists of two lobes, joined in a butterfly-like shape, see Figure 1[3]. The thyroid gland has the task of producing hormones that regulate the body's metabolism – a process to which iodine is essential. Iodine is supplied to the body through dietary intake, and will accumulate in the thyroid gland, where it takes part in the production of thyroid hormones. Thyroid hormones will act on virtually every tissue of the body. Thus, thyroid dysfunction will have extensive physiological impact, affecting the functioning of the brain, heart and other organs.[4]

Thyroid cancer is a malignant tumor that develops in tissues of the thyroid gland. Thyroid cancers are commonly divided into four different groups; papillary, follicular, medullary and anaplastic. This division is based upon the origin and characteristics of the malignancy.[5] Papillary and follicular thyroid cancers are commonly treated with ^{131}I.

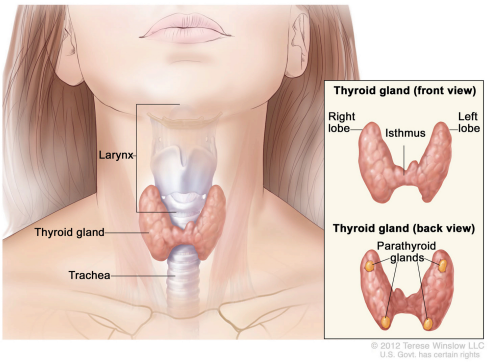

Figure 1: *The anatomy of the thyroid and parathyroid glands.*[3]

After diagnosis, the thyroid is usually removed in its entirety, through a so called thyroidectomy. Thereafter, ^{131}I is given to treat thyroid tissue remnant or suspected residual disease, as well as thyroid cancer metastases. The activities administered at SUS are largely determined based on guidelines published by the American Thyroid Association, ATA. In the 2016 ATA guidelines, the following recommendations are given regarding the administration of ^{131}I;

In patients with low-risk thyroid cancer, or intermediate-risk disease with lower risk features, an approximate ^{131}I activity of 1100 MBq is strongly recommended for remnant ablation, based on what ATA classifies as high-quality evidence. For adjuvant therapy to treat suspected microscopic residual disease, with no distant metastases, an approximate ^{131}I activity of 3700 MBq is recommended. This recommendation however is categorized as weak, supported by low-quality evidence, meaning other alternatives may be equally reasonable. When treating patients with pulmonary micrometastases (< 2 mm), 3700-7400 MBq of ^{131}I, or activities estimated by dosimetry, is strongly recommended. Furthermore, the treatment should be repeated every 6-12 months, as long as a clinical response can be observed. In treatments for macronodular metastases and bone metastases, 3700-7400 MBq of ^{131}I is recommended. These recommendations are however one again considered weak, as other alternatives may be equally appropriate. After treatment, ATA strongly recommends a post therapeutic whole-body gamma scan, with or without SPECT/CT, to inform disease staging and document the iodine uptake of any structural disease.[6]

Consequently, at SUS, the activity administered is either 1100, 3700 or 7400 MBq, depending of stage of the disease. Furthermore, a post therapeutic whole-body scan is performed, and complemented by a SPECT/CT scan if any unusual uptake or new pathology can be observed.

[3] Winslow T. Anatomy of the Thyroid and Parathyroid Glands [Illustration]. 2012. [cited 2019-07-05] Available from: *https://www.teresewinslow.com/head/nmpuvgu8p79zjo65f2wx0i6g7b6du7*
[4] Nussey S, Whitehead S. Endocrinology: An Integrated Approach. Oxford: BIOS Scientific Publishers; 2001. Chapter 3, The thyroid gland. Available from: *https://www.ncbi.nlm.nih.gov/books/NBK28/*
[5] Swedish Cancer Society. Sköldkörtelcancer [Internet]. Stockholm: Swedish Cancer Society; 2018 [updated 2018-11-26; cited 2019-04-18]. Available from: *https://www.cancerfonden.se/om-cancer/skoldkortelcancer*
[6] Haugen BR, Alexander EK, Bible KC, Doherty GM, Mandel SJ, Nikiforov YE et al. 2015 American Thyroid Association Management Guidelines for Adult Patients with Thyroid Nodules and Differentiated Thyroid Cancer: The American Thyroid Association Guidelines Task Force on Thyroid Nodules and Differentiated Thyroid Cancer. Thyroid. 2016;26(1):1–133.

2.2 ^{131}I decay scheme

Iodine-131 decays to various excited states of ^{131}Xe through emission of β- particles, with a half-life of 8.02 days. The most common β- emission (89.4%) has a maximum energy of 606.3 keV, and an average energy of 191.6 keV.[7] In water, this is corresponds to an average path length of approximately 2.3 mm (R_{CSDA} = 0.2265 g/cm² for E = 600 keV).[8]

Furthermore, the disintegration will generate numerous gamma emissions, the most common (81.2%) having an energy of 364.49 keV.[7], giving a half value layer of approximately 6.3 cm (μ/ρ = 0.1105 cm²/g) in water.[9] These are the photons used in imaging with ^{131}I. However, the decay will also yield some high energy emissions, such as 636.99 keV (7.12%) and 722.91 keV (1.79%).[7] In water, these photon energies correspond to a half value layer of 7.9 and 8.3 cm (μ/ρ = 0.0878 and 0.0831 cm²/g), respectively.[9] Although relatively few in number, these higher-energy emissions can produce rather immense difficulties in ^{131}I imaging and quantifications. This will be discussed in greater detail further on.

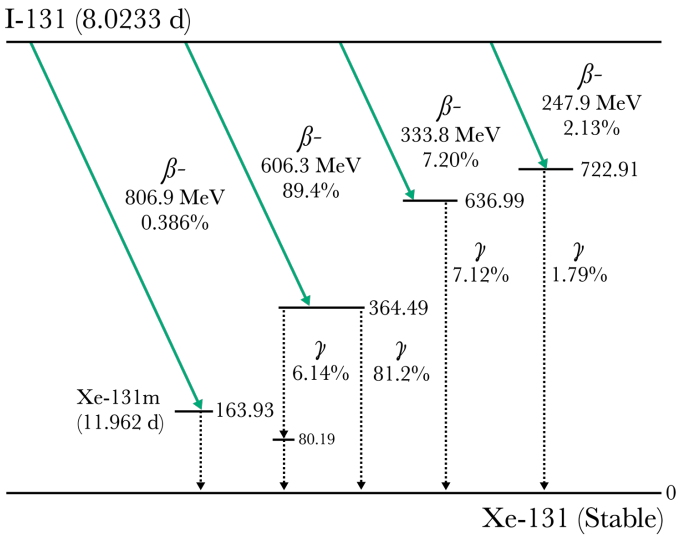

Figure 2: *Reduced decay scheme for ^{131}I.*

[7] Laboratoire National Nehri Becquerel. Atomic and Nuclear data, I-131 table. [Internet] Gif-sur-Yvette Cedex, France: Laboratoire National Nehri Becquerel; 2001 - . [updated 2014-01-20; cited 2019-04-20]. Available from: *http://www.lnhb.fr/nuclides/I-131_tables.pdf*

[8] NIST. ESTAR: Stopping Power and Range Tables for Electrons. [Internet] Gaithersburg, USA: National Institute of Standards and Technology; 1998 - . [updated July 2017; cited 2019-07-05]. Available from: *https://physics.nist.gov/cgi-bin/Star/e_table.pl*

[9] NIST. X-ray Mass Attenuation Coefficents. [Internet] Gaithersburg, USA: National Institute of Standards and Technology; 1998 - . [updated July 2004; cited 2019-07-05]. Available from: *https://physics.nist.gov/PhysRefData/XrayMassCoef/ComTab/water.html*

2.3 Basic gamma imaging principles

2.3.1 The gamma camera: An overview

The gamma camera is a device used in nuclear medicine imaging to detect photons emitted by a radiopharmaceutical. Principal components are the detector medium, collimator, photomultiplier tubes, as well as other signal processing electronics. In this chapter, the functions of the gamma camera will be explained in further detail. For a schematic illustration of the device, see Figure 4.

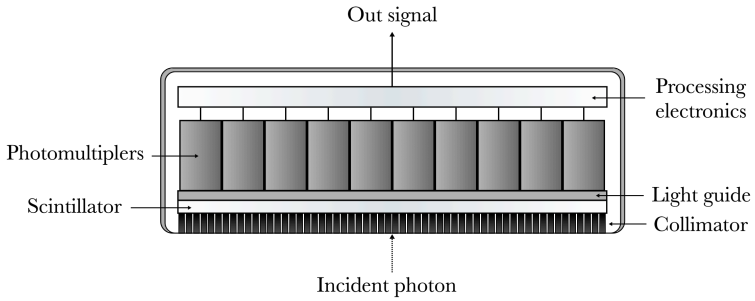

Figure 4: *Schematic illustration of the gamma camera head.*

The gamma camera consists of one or several detector heads, containing the different detector components. The perhaps most important component is the detector itself. In modern systems, various detector materials are used to detect the incident photons. Traditionally however, the detection principle has been based on the phenomena of scintillation, using a scintillation crystal as the detector medium. Incident photons will interact with the crystal, and thereby release electrons. The kinetic energy of the electrons will be absorbed by the crystal, causing it to enter an excited state. As the crystal deexcites, visible light is emitted, in the form of scintillation photons. The light intensity is proportional to the energy imparted.[10]

In order to give the incoming signal a spatial dependency, a collimator is mounted in front of the crystal. A collimator is a block of highly attenuating material, usually lead, equipped with holes and septa in a specific geometric pattern. This will allow only the photons traveling in the desired direction (i.e. perpendicularly to the detector surface) to enter the device and absorb in the crystal, while photons travelling at an angle will be absorbed by the septa. The properties of the collimator is determined by the design of the holes and septa, i.e. the hole length, hole diameter and septal thickness. In imaging with high-energy nuclides such as ^{131}I, there is an increased risk for septal penetration, meaning photons will travel through the septa and register in the detector. This will reduce image contrast and induce artifacts. To minimize these effects, a so called high-energy collimator is used. High-energy collimators have thick septa, to produce a lower transparency to high-energy photons, which will minimize septal penetration. Furthermore, the collimator used in ^{131}I imaging is a so called parallel-hole collimator, meaning holes and septa are parallel to each other. This will generate an image in which projected structures are true to size, with no magnification or geometric distortion.[11]

The scintillation crystal is coupled to a number of photomultiplier tubes through a light guide. On entering the photomultiplier tube, photons will interact with a photocathode and thereby release photoelectrons. The emitted electrons are focused towards a series of dynodes, which will amplify the signal. The electrons are then collected with an anode, converted into pulses and processed through a number of electronic components. The proportionality between the energy deposited in the crystal is preserved throughout the process. Therefore, the output signal will carry information regarding both the position of and energy deposited in the interaction, enabling the image formation. The result is a two-dimensional image, depicting the distribution of radiopharmaceutical.[11]

[10] Knoll GF. Radiation Detection and Measurement. 4th edition. USA: Wiley; 2010.
[11] Khalil MM. Basic Sciences of Nuclear Medicine. Berlin Heidelberg: Springer-Verlag; 2011. 10, Elements of Gamma Camera and SPECT Systems. p. 155-78.

2.3.2 SPECT imaging: Acquisition and reconstruction

Single Photon Emission Computed Tomography, SPECT, is a three-dimensional derivative of planar gamma camera imaging. The two techniques are based on the same basic principles, however, the construction of three-dimensional images requires a different approach with regards to image acquisition and formation, which will be discussed in this chapter.

In planar imaging, images are obtained by measuring in one single view. Hence, the acquired image is a two-dimensional projection of a three-dimensional object, and does consequently not contain any information regarding depth. This may present problems, as activity located on same line of projection will be superimposed in the acquired image.[12]

In SPECT imaging, a three-dimensional image is obtained by measuring in several angles around the examined object, thereby generating a number of projections, see Figure 5. Measured projections can, by using a reconstruction algorithm, be turned into a three-dimensional image.[12]

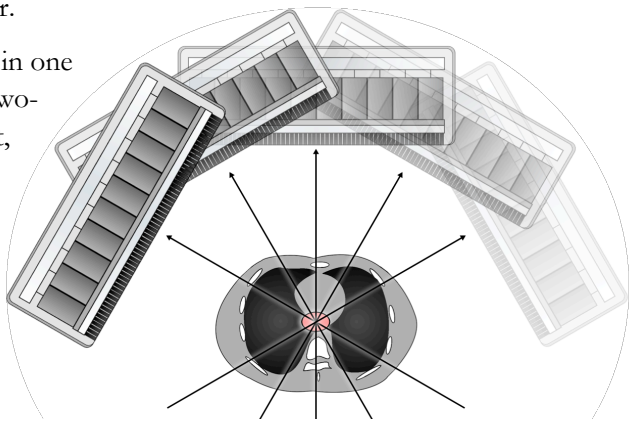

Figure 5: *SPECT acquisition. Data is acquired by rotating one or multiple gamma camera heads around the patients, measuring projections at a several angles.*

In modern SPECT systems, images are usually reconstructed using iterative reconstruction algorithms. The key feature of these algorithms is that the reconstruction begins with an initial estimate of the source distribution, from which projections are calculated. Calculated projections are then compared to measured projections. Based on the difference between the two, the estimated source distribution can be updated. The process is repeated until an image of satisfactory quality is attained. For the entire chain of formation, see Figure 6.[13]

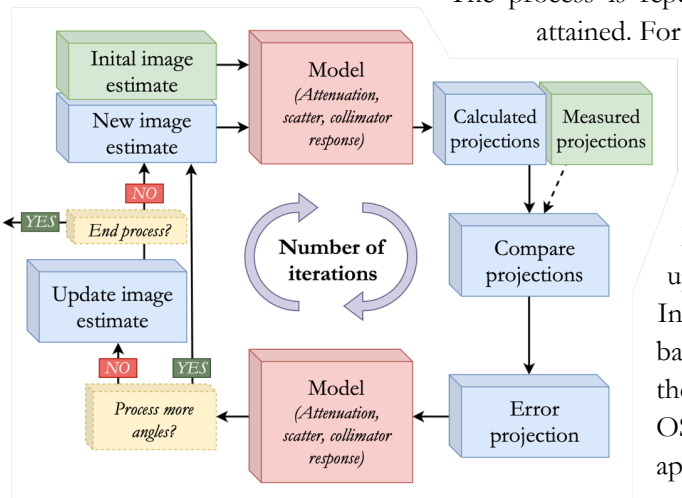

Figure 6: *Image formation in an iterative reconstruction algorithm.*

There are two principal iterative reconstruction methods; Maximum Likelihood Expectation Maximization (*ML-EM*) and Ordered Subsets Expectation Maximization (*OS-EM*). In an ML-EM reconstruction, the image is not updated until all projections have been processed. In OS-EM however, the image estimate is updated based on a subset of projections. This will increase the speed of the image formation. For this reason, OS-EM is commonly used in clinical applications.[13]

[12] Bruyant PP. Analytic and Iterative Reconstruction Algorithms in SPECT. J Nucl Med. 2002 Oct;43(10):1343-58.
[13] Ljungberg M, Pretorius PH. SPECT/CT: an update on technological developments and clinical applications. Br J Radiol. 2018 Jan; 91(1081): 20160402.

2.4 Gamma camera performance characteristics

In this chapter, important characteristics of the gamma camera will be discussed. Gamma camera characteristics are commonly divided into two different categories; intrinsic and extrinsic. The intrinsic properties of a gamma camera relates to components within the camera, such as the crystal, photomultiplier tubes and other electronics, while extrinsic properties also include external variables such as the collimator and image display.

2.4.1 Spatial resolution

The spatial resolution of a gamma camera is derived of two parameters; the intrinsic resolution R_I and the collimator resolution R_C.

The collimator resolution can be defined as the full-width half maximum (*FWHM*) of the profile projected by a point source. R_C will depend on the hole length *l* and hole diameter *d*, as well as the source-to-collimator distance *b*, see Figure 7. As the collimator resolution is poor in comparison to the intrinsic resolution, the system resolution is largely defined by these parameters. The collimator resolution can be approximated as follows:

$$R_C \approx \frac{d(l_e + b)}{l_e} \quad (1)$$

Where l_e is the effective length of the collimator hole, defined as $l_e = l - 2/\mu$, where μ is the linear attenuation coefficient of the collimator material.[14]

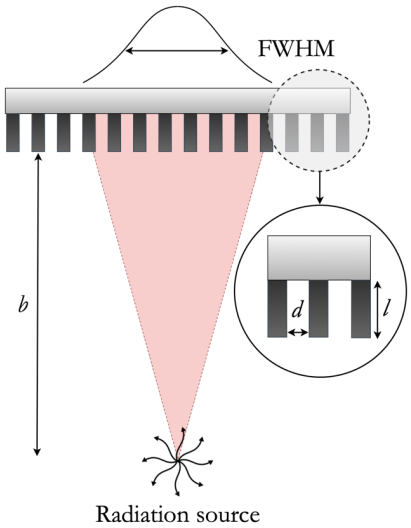

Figure 7: *Collimator resolution. The FWHM of the projected profile will depend on the length l and width d of the collimator hole, as well as the source-to-collimator distance b.*

Imaging with ^{131}I is commonly performed using a High Energy General Purpose (*HEGP*) collimator. HEGP collimators have thick collimator walls to minimize septal penetration. Furthermore, the hole diameter *d* is large, giving a large hole separation. This will broaden the FWHM of the projected profile, and result in poor resolution.[14]

In addition, the resolution depends on the source-to-collimator distance *b*. As *b* increases, photons are able to enter the detector through more collimator holes, which will broaden the FWHM. The FWHM of a projected point source will depend approximately linearly on the distance to the source. This relationship is referred to as the collimator-distance response (*CDR*) function. [14]

[14] Sorenson JA, Phelps ME. Physics in Nuclear Medicine. 2nd ed. United States; Elsevier; 1987. 16; The Anger Camera: Performance Characteristics. p. 331-45.

2.4.2 Sensitivity

The sensitivity is a parameter that connects the relative response of a nuclear imaging system to a given amount of activity. It is commonly defined as the observed count rate per unit radioactivity for a given source and measurement geometry.[15]

The sensitivity depends on several factors, such as the thickness of the scintillation crystal and the signal processing electronics. However, the design of the collimator is once again a critical factor. Good sensitivity can be obtained by using a collimator with large collimator holes and thin collimator walls. Unfortunately, such a design will compromise the image resolution and increase the risk of septal penetration. Therefore, these effects must be considered when choosing the collimator design. [14]

It is important to note that the sensitivity of a gamma camera is independent of the distance b from the source to the face of the collimator. As b increases, the photon flux is reduced, which lessens the number of counts detected per unit area. However, an increased distance b will increase the acceptance angle, which allows photons to be detected across a larger detector space. These effects will counteract, making the sensitivity remain constant, see Figure 8.[14]

The invariance in detection efficiency only applies to primary photons, as septal penetration and photon scattering will separately contribute to the counts measured. The amount of septal penetration will increase exponentially as the distance to the source decreases – making a quite large contribution at short distances. Consequently, when septal penetration and scatter is present (as it certainly is in imaging with high-energy nuclides as ^{131}I), the recorded count rate will vary with the distance to the source.

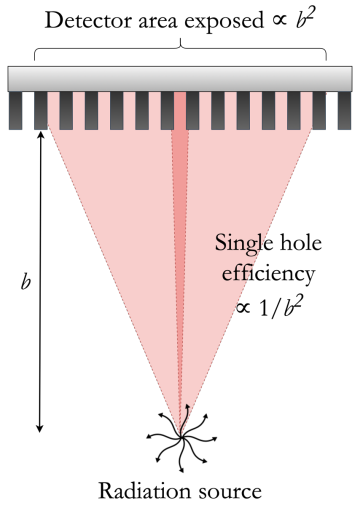

Figure 8: *Illustration of the detection efficiency. The single hole efficiency is proportionate to $1/b^2$, while the number of holes exposed is proportionate to b^2. The total detection efficiency will therefore be independent of the distance b.*

2.4.3 Uniformity

Image uniformity refers to the consistency of the response across the image field of view (*FOV*). The uniformity of a nuclear imaging device is of great importance in both qualitative and quantitative measures. Once again, uniformity can be categorized as intrinsic or extrinsic. Intrinsic non-uniformities will, for instance, arise from defects in the scintillation crystal or inadequate calibration of the photomultiplier tubes. Furthermore, the intrinsic uniformity of a gamma camera will also vary depending on the energy of the isotope, as well as the energy window used.[16] The extrinsic uniformity will, in addition, depend on the collimator. If the pattern of holes and septa is non-uniform, non-uniformities will be induced in the acquired image. Furthermore, non-uniformities may also be induced in image reconstruction, as corrections for attenuation and unwanted events also effects the uniformity of a reconstructed image.[15]

[15] NEMA. Performance Measurements of Gamma Cameras. Rosslyn: National Electrical Manufacturers Association; 2007.
[16] IAEA. Nuclear Medicine Physics: A Handbook for Teachers and Students. Vienna: International Atomic Energy Agency; 2014.

2.5 Quantitative SPECT

In quantitative SPECT, the aim is not only to visualize the activity uptake, but to generate images with a count distribution that accurately corresponds to true activity within the examined object. While images acquired in clinical settings may be suitable for diagnostic procedures, this does not guarantee accuracy in quantifications measures. Projection data may still be severely degraded by factors such as attenuation and scatter. Due to the comprised image quality, SPECT used to be considered a non-quantitative imaging modality. However, as the technique has evolved, more superior methods of reconstruction and correction has become available, making accurate SPECT quantifications feasible. Nevertheless, it is very much essential that degrading factors are carefully considered and corrected for, especially in imaging with high-energy radionuclides such as ^{131}I, as the high-energy emissions will further compromise the image quality.[17]

In this chapter, degrading factors and corresponding methods for correction will be discussed. The image formation chain in quantitative SPECT is illustrated in Figure 9.

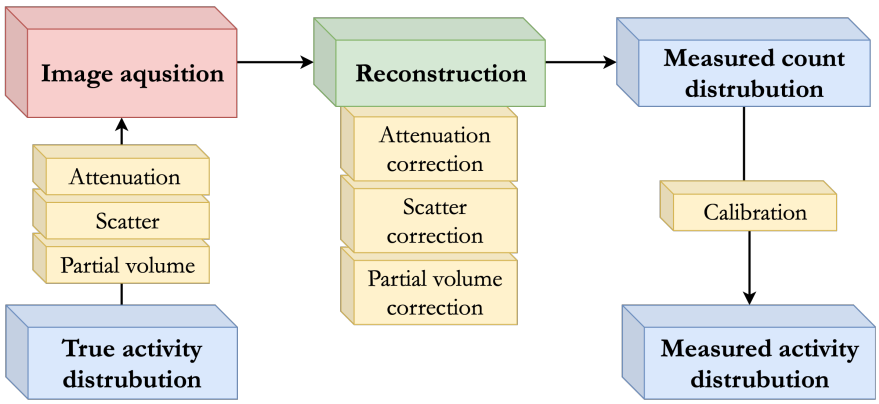

Figure 9: *Image formation in quantitative SPECT.*

2.5.1 Photon attenuation

Reduction in photon fluence due to interactions with matter, i.e. scattering or absorption, is referred to as attenuation. Attenuation can be quantified in terms of linear attenuation coefficients, μ, describing the probability per unit path length of a photon being scattered or absorbed. The level of attenuation will vary depending on the energy of the incident photon, as well as the density and composition of the absorber. The number of incident photons N_0 will, by travelling the distance x in a material with the linear attenuation coefficient μ, be reduced to N as follows:

$$N = N_0 \cdot e^{-\frac{\mu}{\rho}\rho \cdot x} \tag{2}$$

Due to attenuation, the likelihood for detection in nuclear imaging will depend both on the depth of the decay, as well as the attenuation properties of the object. Decays that occur at great depths, surrounded by highly attenuating material, are less likely to be detected, and vice versa. Hence, if not compensated for, attenuation will greatly reduce the measured count rate, and induce very significant artefacts in reconstructed SPECT images.[17]

[17] Ritt P, Vija H, Hornegger J, Kuwert T. Absolute Quantifications in SPECT. Eur J Nucl Med Mol Imaging. 2011 May;38 Suppl 1:S69-77.

The probability *P* for a photon emitted at depth *d* (in a direction towards the detector) to reach the detector at position *D*, can be expressed as:

$$P = \exp\left(\int_d^D -\mu(r)dr\right) \tag{3}$$

The integral represents all linear attenuation coefficients along the vector *r*, that is, from the origin of the decay to the supposed detection site.[17]

To accurately compensate for attenuation, the spatial distribution of the attenuation coefficients within the examined object must be known. This information can be acquired with a CT scan. By converting pixel values in the CT image from Hounsfield units to linear attenuation coefficients, the probability for attenuation along each projection line can be calculated, and integrated in the forward projection of the SPECT reconstruction. Attenuation can thereby be compensated for.[17]

2.5.2 Photon scatter

Scattering occurs when the incident photon interacts with an electron in the absorbing material. The photon will transfer some of its energy to the electron, causing the electron to be ejected and the photon to deflect from its path. Scattered photons can cause problems in gamma camera imaging. The problem lies within the detectors inability to accurately determine the energy imparted in the crystal. The signal will have statistical error, which will cause the photopeak in the energy spectrum to broaden. In order for true events to be recorded, one selects a window of energies, in which primary photons can be detected. However, this will inevitably allow for photons that scatter with an energy close to that of the photopeak to also be detected within the given energy window, and thereby be interpreted as primary photons. These contributions will degrade the image contrast, and may induce significate errors in activity quantification procedures. Therefore, in gamma camera quantifications, photon scattering must be adequately accounted for.[18]

The relationship between energy transfer and the angle of deflection in scatter interactions is described by the Compton equation.[10]

$$h\nu' = \frac{h\nu}{1 + \frac{h\nu}{m_0 c^2}(1 - \cos\theta)} \tag{4}$$

Where $h\nu$ is the incident photon energy, $h\nu'$ is the scattered photon energy, θ is the deflection angle and m_0c^2 is the rest mass of the electron. Furthermore, the probability for photons to scatter at a certain angle, is described by the Klein-Nishina formula.[10]

$$\frac{d\sigma}{d\Omega} = \left(\frac{r_0^2}{2}\right)\left(\frac{h\nu}{h\nu'}\right)^2\left(\frac{h\nu}{h\nu'} + \frac{h\nu'}{h\nu} - 1 + \cos^2\theta\right) \tag{5}$$

Where r_0 is the classical electron radius. The Klein-Nishina formula reveals a strong tendency for forward scattering in interactions with high energy photons. Furthermore, the relative loss of energy in high energy photons interactions will be large, and scattered photons will therefore have a significantly lower energy than incident photons.[10] Hence, in ^{131}I imaging, scattered photons will greatly contribute to the counts recorded in the primary photon window, due to contribution from the higher-energy emissions (such as 637 keV and 723 keV).

[18] Ljungberg M. Quantitative SPECT Imaging. In: Khalil MM, editor. Basic Sciences of Nuclear Medicine. Berlin Heidelberg: Springer-Verlag; 2011. p. 285-309.

In this work, two window-based scatter correction methods will be examined, namely the Dual Energy Window (*DEW*) method[19] and the Triple Energy Window (*TEW*) method[20]. In these methods, additional energy windows are used to record scattered photons. This data is later used to subtract events from the primary energy window. This principle is illustrated in Figures 10 A-B). The gamma spectrum seen in Figures 10 A-B) was acquired through Monte-Carlo simulations of ^{131}I, dispensed in a water-filled Jaszczak phantom, and recorded with a NaI(Tl)-detector. The true (i.e. simulated) scatter component is marked in blue, and the scatter component provided by the correction is marked in yellow.

In the DEW method, one broad energy window is set up below the photopeak window, see Figure 10 A). Scattered corrected projections are calculated as:[18]

$$P(x,y) = P(x,y)_{peak} - k \cdot P(x,y)_{left} \tag{6}$$

Where $P(x,y)_{peak}$ and $P(x,y)_{left}$ are the image acquired using the photopeak window and the scatter window, respectively, and k is a scaling factor. In the TEW method, two adjacent energy windows, with width ΔE_{left} and ΔE_{right}, are set up around the photopeak window, see Figure 10 B). The corrected projections are generated as follows:[18]

$$P(x,y) = P(x,y)_{peak} - \left(\frac{P(x,y)_{left}}{\Delta E_{left}} + \frac{P(x,y)_{right}}{\Delta E_{right}}\right) \cdot \frac{\Delta E_{peak}}{2} \tag{7}$$

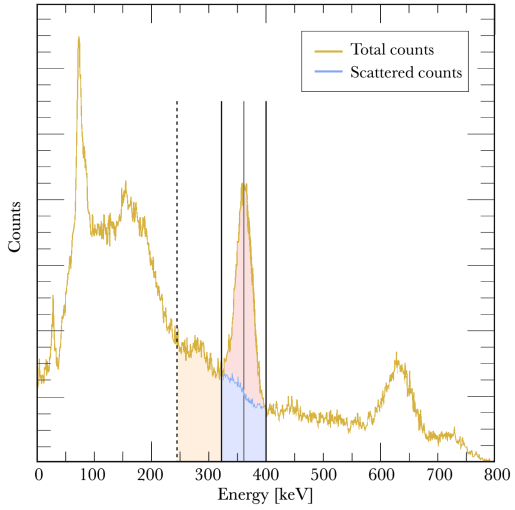

Figure 10 A): *Dual Energy Window correction. The scatter component in the photopeak is approximated using a lower, adjacent energy window.*

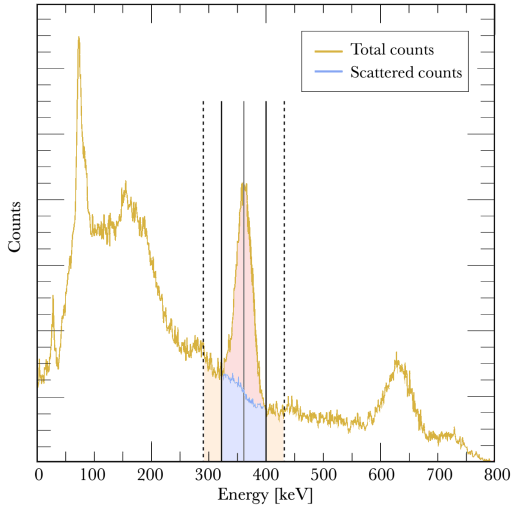

Figure 10 B): *Triple Energy Window correction. The scatter component in the photopeak is approximated using two adjacent energy windows.*

[19] Jaszczak RJ, Greer KL, Floyd CE Jr, Harris CC, Coleman RE. Improved SPECT quantification using compensation for scattered photons. J Nucl Med. 1984 Aug;25(8):893-900.
[20] Ogawa K, Harata Y, Ichihara T, Kubo A, Hashimoto S. A practical method for position-dependent Compton-scatter correction in single photon emission CT. IEEE Trans Med Imaging. 1991;10(3):408-12.

2.5.3 Collimator penetration

Collimator penetration, or septal penetration, occurs when photons manage to penetrate the collimator walls, and be detected at a site further away than that defined by the collimator hole. In SPECT imaging septal penetration will, much like scatter, reduce image contrast and degrade the overall image quality. Naturally, as high-energy photons have more penetrating power, collimation penetration is more prominent in imaging with high-energy nuclides, such as ^{131}I. Hence, in quantitative SPECT with high-energy nuclides, the effects of collimator penetration must be carefully considered.[18]

The probability for penetration will depend on the angle of the incident photon. A large incident angle will result in a shorter path length through the collimator walls, making penetration more likely. As collimator holes are arranged in a hexagonal geometry, there will be six angles for which penetration is more likely. In planar imaging, septal penetration will therefore manifest as a star-like pattern, see the Figure 11. For sources located close to the detector, a larger fraction of the photons emitted are able to enter the detector at a large angle, resulting in a higher probability for penetration. Consequently, when penetration is present, a source-to-collimator distance dependence is introduced to the count rate, which may complicate quantification procedures. [18,21]

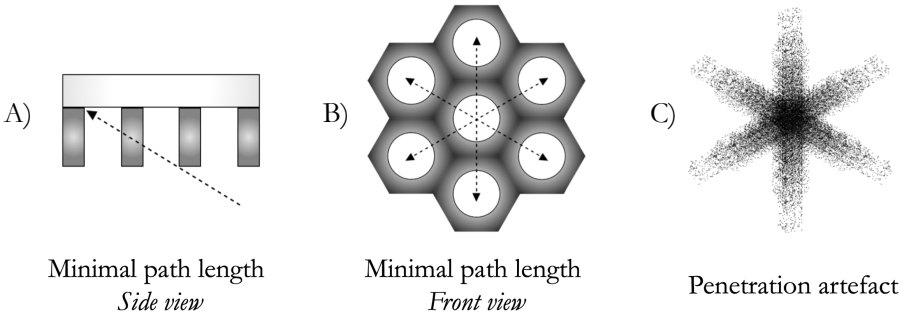

Figure 11 A-C): *Illustrations of the principles behind septal penetration. Penetration is most likely to occur when the photons path through the absorber is minimized, see illustration A-B). Due to the hexagonal geometry of the collimator holes, penetration can induce a star-shaped pattern in planar images, see illustration C).*

The amount of septal penetration can be reduced by increasing the thickness of the septa. However, this entails either increasing the hole separation, or decreasing the hole diameter. Increasing the hole separation will degrade the spatial resolution, while decreasing the hole diameter will decrease the system sensitivity. Hence, spatial resolution, system sensitivity, and risk for penetration is in direct conflict when constructing a collimator. No design is optimal – a trade-off is inevitable.[21]

In NEMA NU 2-2007[15], a method for quantifying the fraction of penetration detected in a measurement is provided. According to this standard, the penetration factor *PF* (i.e. the fraction of penetration) can be quantified by fitting count rates *R*, recorded at different source-to-collimator distances *D*, to the exponential function below using a non-linear least square fit technique.[15]

$$R_i = c_0 + c_1 e^{-c_2 D_i} \tag{8}$$

By extracting the fitting parameters c_1, c_2 and c_3, the *PF* at a given distance D_N can be calculated as follows:[15]

$$PF = \frac{c_1 e^{-c_2 D_N}}{c_0 + c_1 e^{-c_2 D_N}} \tag{9}$$

It should be noted that this applies to in-air measurements of a petri dish.

[21] Gunter DL. Collimator Design for Nuclear Medicine. In: Wernich MN, Aarsvold JN, editors. Emission Tomography: The Fundamentals of PET and SPECT. San Diego, California, USA: Elsevier; 2004. p.160-61.

2.5.4 Partial volume effects and collimator detector response

As previously discussed, the resolution of a nuclear imaging device is limited by both extrinsic and intrinsic parameters. Effects that arise from the limited spatial resolution of the imaging device are referred to as partial volume effects (*PVE)*. PVE will cause blurring, making structures appear larger and dimmer, as well as reduce the contrast between hot regions and background. Hence, in tumor imaging, PVE will affect both the apparent size and uptake of a lesion.[22]

The amount of degradation due to PVE will not only depend on the spatial resolution of the imager, but also the source activity distribution. Pixels located on the edges of a source will include signal from both source, as well as the background. The signal intensity in these pixels will be therefore be a mean of the different signal intensities.[23] As quantifications measures generally requires the origin of the activity to be delineated, PVE may induce errors through what is referred to as spillover effects. Spill-*in* effects occur when activity originating from outside the studied structure leaks into the ROI, increasing the counts measured, resulting in an overestimation of activity. On the contrary, the measured activity may be underestimated in cases where the source activity is distributed over the boarders of the ROI, that is due to spill-*out* effects. For a heterogenous activity distributions, spillover effects can result in significant quantification errors.[17]

There are a few different methods that can be used to compensate for PVE. As previously mentioned, the spatial resolution of gamma camera images can by heavily degraded by the spatially varying collimator-detector response, CDR. Luckily, as SPECT acquisitions will provide information regarding the collimator-source distance, the CDR can be modelled and compensated for in the image reconstruction, thereby improving the image quality. However, CDR corrections will not fully recover the loss of resolution. For small structures, the loss of resolution may still be significant.[22]

A common method of PVE correction includes the use of so-called recovery coefficients (*RC*). RC's are commonly used to characterize the resolution of nuclear images. The RC's represent the ratio between apparent activity and true activity, and will depend on the activity concentration of the structure as well as the surrounding background. RC's can be obtained by measuring activity of known volume and concentration, for example a known activity concentration dispensed in different sized spheres. Hence, RC can be expressed as a function of volume, allowing for measured activities to be corrected with regards to apparent size. This method is both simple and efficient when correcting for spillover effects due to PVE. However, it does require assumptions to be made regarding the size, shape and homogeneity of the lesion, as well as with regards to background activity levels.[22]

[22] IAEA. Quantitative Nuclear Medicine Imaging: Concepts, Requirements and Methods. Vienna: International Atomic Energy Agency; 2014. IAEA Human Health Series, ISSN 2074; no. 9.
[23] Soret M, Bacharach SL, Buvat I. Partial-Volume Effect in PET Tumor Imaging. J Nucl Med 2007; 48:932–945.

2.5.6 Calibration

Although adequate methods of correction should largely recover the activity in reconstructed SPECT images, one still needs to consider remaining effects related to the specific circumstances of the measurement. This is done through calibration measurements, and the use of so-called calibration factors. The calibration factor (typically in units of cps/MBq) will provide the relationship between count rate and activity for specific measurement. It is also commonly referred to as the system sensitivity. However, calibration factors differs from sensitivity in the since that they depends on additional factors, such as acquisition and reconstruction parameters, methods of compensation and measurement geometry.[22]

Calibration measurements can be performed in numerous different fashions. The main principle remains the same - a known activity (quantified with an accurate dose calibrator) is imaged, and the calibration factor is calculated by dividing the observed count rate in a specific region by the true activity in that very region. The perhaps most basic calibration measurement would be a planar, in-air acquisition with a point-like source, assuming negligible scatter and attenuation. However, the use of such calibration factors require a sophisticated reconstruction of imaging data, using highly accurate methods of correction. As previously discussed, ^{131}I images can suffer a high level of degradation due to the high energy of the photon emissions. Perfect corrections are very difficult to attain. Hence, in ^{131}I quantifications, a more refined calibration is called for. [24,25]

In quantitative SPECT, the calibration factor should ideally be determined through a SPECT acquisition, using a set-up that as closely as possible resembles the patient geometry and activity distribution. However, in a clinical setting, this procedure would be rather impractical, as patients will vary in size, shape, and most importantly – with respect to the ^{131}I uptake and distribution. A more suitable approach is to use a source geometry that approximates the attenuation and scatter properties in patients, such as a cylindrical tank with uniform activity, either with or without hot inserts. Furthermore, the acquisition, reconstruction, compensation and target definition in the calibration study should be performed in the same manner as in the corresponding patient study. To improve the precision of the calibration factor, the acquisition time may be extended, compared to in patient imaging.[24,25]

The calibration of the system volume sensitivity can be calculated as;

$$S = \frac{R}{V \cdot C} \cdot K \tag{10}$$

Where R is the measured count rate, V is the volume of the defined region, C is the true activity concentration within that region at time T_0, and K is a decay constant. The decay constant is used to correct for the radioactive decay from the from T_0 to the time of the calibration, and can be determined as follows;

$$K = e^{(T_0 - T_{cal}) \cdot \lambda} \cdot \left(T_{acq} \cdot \lambda\right) \cdot \left(1 - e^{-T_{acq} \cdot \lambda}\right)^{-1} \tag{11}$$

Where T_{cal} denotes the elapsed time from T_0 to the start of the measurement, T_{acq} is the time of acquisition and λ is the decay constant for the radionuclide in question.[17]

Once a calibration factor has been established, the apparent activity can be calculated as;

$$A = \frac{R}{S} \tag{12}$$

Where R is the recorded count rate within the defined region.

[24] Dewaraja YK, Frey EC, Sgouros G, Brill AB, Roberson P, Zanzonico PB, et al. MIRD Pamphlet No. 23: Quantitative SPECT for Patient-Specific 3-Dimensional Dosimetry in Internal Radionuclide Therapy. J Nucl Med 2012; 53:1310-1325.
[25] Dewaraja YK, Ljungberg M, Green AJ, Zanzonico PB, Frey EC, SNMMI MIRD Committee, et al. MIRD Pamphlet No. 24: Guidelines for Quantitative 131I SPECT in Dosimetry Applications. J Nucl Med. 2013;54:2182-2188.

3 Material and method

3.1 Phantom studies and measurements

A Capintec CRC®-55tR Dose Calibrator, calibrated to ^{131}I dispensed in a plastic mug with 25 mL water, was used to measure activities.

All image acquisitions were performed using a Discovery NM/CT 670 SPECT/CT scanner (GE Healthcare) with a HEGP, parallel-hole collimator. The GE Xeleris workstation was used to display and process images. Measurements were performed using standard clinical ^{131}I acquisition protocols, see Table 1-3, with some adjustments depending on the measurement. Adjustments will be specified. Furthermore, SPECT reconstructions were performed using the GE application Volumetrix MI. Clinical reconstruction parameters are presented in Table 4.

Table 1: *SPECT acquisition parameters.*

Detector mode	H (Two opposing detector heads)
Body contouring	On
Axial FOV [cm]	40
Angular range [°]	360 (180° per detector)
Number of views	60 (6° per step)
Time [s]	45 per projection
Matrix size [pixels]	128 x 128
Voxel size [mm^3]	0.4428 x 0.4428 x 0.4428
Energy window	364 keV ± 10%

Table 2: *CT acquisition parameters.*

Scan type	Low-dose helical
Voltage [kV]	120
Current [mA]	30-80 (Smart)
Slice thickness [mm]	3.75
Pixel size [mm^2]	1.25 x 1.25

Table 3: *Static acquisition parameters.*

Body contouring	On
Axial FOV [cm]	40
Acquisition time [s]	600
Matrix size [pixels]	256 x 256
Pixel size [mm^2]	0.2214 x 0.2214
Energy window	364 keV ± 10%

Table 4: *Clinical reconstruction settings.*

Iterative Reconstruction (*IR*)	OSEM 4i10s
Attenuation Correction (*AC*)	On
Resolution Recovery (*RR*)	On
Scatter Correction (*SC*)	None
Post-reconstruction filtering	On

Table 5: *Energy window settings.*

Window	Interval [keV]	ΔE [keV]
Photopeak Window (*EM*)	328-400	72 (20%)
Dual Energy Window (*DEW*)	267-327	60 (16.5%)
Triple Energy Window (*TEW*)	315-324 + 404-420	9 (2.5%) + 15 (4%)

It should be noted that the standard acquisition protocols (see Tables 1 and 3) only included one energy window, i.e. that centered around the photopeak (364 keV ± 10%). In order to enable the scatter correction, additional windows had to be set up. Firstly, a preexisting DEW (297 keV ± 10%), provided by the manufacturer, was added to the protocol.

As the Xeleris version used provided no option for TEW corrections, the TEW projections had to be constructed using a separate application. To allow for that, the entire spectrum was recorded in list mode. The list mode data was then exported, and TEW projections were calculated using IDL, with Eq. (7). The energy window settings chosen for the TEW correction are presented in Table 5. The calculated projections were then compiled into DICOM files, and reuploaded to Xeleris. By doing so, the TEW correction could be incorporated into the SPECT reconstruction, which could be performed per usual (i.e. using Volumetrix MI). In planar scatter corrections, the correction was performed by subtracting the calculated TEW projections from the acquired images – once again using the Xeleris workstation. In short, the TEW projections were created using a separate application, however, all scatter corrections were performed using tools available in Xeleris.

3.1.1 Planar sensitivity and penetration

The purpose of this study was to determine the planar sensitivity for the system, as well as to establish calibration factors for planar quantifications. Furthermore, measurements was performed to assess the penetration contribution at different source-to-collimator distances.

An ^{131}I activity of 51.4 MBq was dispensed into a petri dish (∅ = 9 cm). Firstly, a measurement of planar sensitivity was performed. The dish was positioned parallel to the plane of the detector, near the center of the FOV. The detector was positioned so that the distance between the face of the collimator and the surface of the ^{131}I solution measured d = 100 mm, see Figure 12. The activity was then measured for 600 seconds. The measurement was repeated for the second detector.

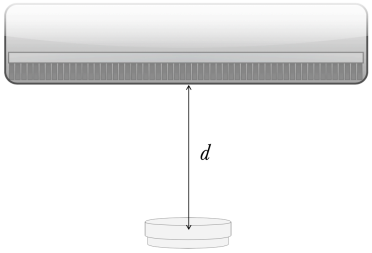

Figure 12: *Measurement set-up.*

Acquired images were corrected for scatter, giving the image sets (*no SC + DEW + TEW*). The system sensitivity was determined by dividing the total count rate by the total activity. The average count rate within a small ROI (∅ = 1 cm) centered over the dish, was determined, and calibration factors were calculated using Eq. (10).

Penetration measurements were performed using the same set-up. The detector was positioned directly above the dish, so that surface of the ^{131}I solution was at a 10 mm distance from the face of the collimator. The petri dish was measured for 300 seconds. The measurement was repeated at distances d = 20, 50, 150, 200, 250, 300, 350 and 400 mm.

Acquired images were corrected for scatter, once again giving the image sets (*no SC + DEW + TEW*). For each image in each set, a small circular ROI (∅ = 26 mm, i.e. approximately 30% of the petri dish diameter) was defined close to the center of the petri dish. The count rate within the ROI's was determined, and plotted as a function of d. For the non-scattered corrected images, the count rates were fitted to an exponential function, and penetration factors was determined as described in Eq. (8) and (9).

3.1.2 Scatter measurements

This study aimed to assess the effectiveness of TEW and DEW scatter corrections in planar measurements.

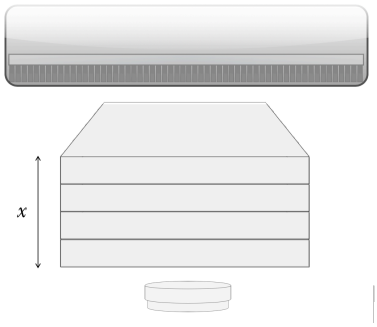

Figure 13: *Measurement set-up.*

An ^{131}I activity of 52.8 MBq was dispensed into a petri dish (∅ = 9 cm). The dish was placed in a PMMA stand, consisting of a block of PMMA, with a circular cut-out the same size as the dish. The detector was positioned parallel to the surface of the dish, with a source-to-collimator distance of d = 25 cm. Blocks of PMMA was successively stacked on top of the dish, while planar measurements were performed, giving a PMMA thickness x ranging from 0 to 20 cm, see Figure 13.

In order to achieve the same statistical certainty in all measurements, the time of acquisition t was extended to account for the attenuation in the PMMA blocks. This was done using the attenuation formula, see Eq. (2), using E = 364.49 keV, ρ = 1.18 g/cm^3, μ/ρ = 0.1074 cm^2/g and t = 300 s at x = 0 .

Acquired images was corrected for scatter. For all images, the total count rate for the plane was determined, and plotted as a function of x. In addition, the count rate within a small ROI (∅ = 3.75 cm) at the center of the dish was determined and plotted as a function of x.

3.1.3 System volume sensitivity and calibration

The purpose of these measurements were to determine the system sensitivity, and to establish calibration factors for further SPECT quantifications.

Measurements were performed using a Jaszczak SPECT Phantom. The phantom has a cylindrical shape, and a disposable volume of 6.8 L, see Figure 14. No inserts were used. The phantom was filled with 6795 mL of water. 206.2 MBq of ^{131}I was dispensed in the phantom, giving a activity concentration of 30.4 MBq/L. SPECT measurement was performed using the clinical standard protocol, but with an extended acquisition time of 90 s per view. Acquired projection data was reconstructed using the reconstruction settings presented in Table 6, giving three images; No SC (*IRACRR*) + DEW (*IRACSCRR*) + TEW (*IRACSCRR*).

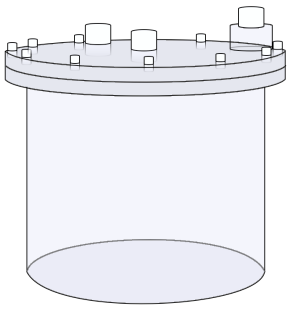

Figure 14: *Illustration of the Jaszczak phantom.*

The system volume sensitivity was determined by dividing the total count rate by the total activity. The SPECT calibration factors were calculated with Eq. (10), using the recorded count rate within a spherical VOI (∅ = 11 cm) positioned close to the center of the phantom.

Table 6: *Clinical reconstruction settings.*

IR	OSEM 4i10s
AC	On
RR	On
SC	None + DEW + TEW
Filtering	Off

3.1.4 NEMA measurements

The aim of these measurements was to study partial volume effects and to establish recovery coefficients for the upcoming quantifications.

Measurements were performed using a NEMA 2012/IEC 2008 Body Phantom, see Figure 15. The phantom has a disposable volume of approximately 10 L, and contains six fillable spheres with diameters of 10, 13, 17, 22, 28 and 37 mm.

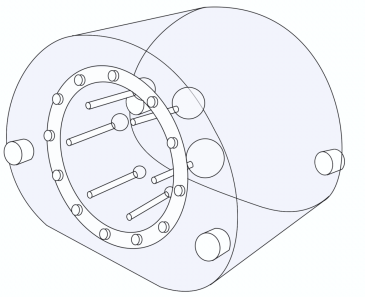

Figure 15: *Illustration of the NEMA phantom.*

A 70.0 kBq/mL solution of ^{131}I was prepared and dispensed into the spheres. No other inserts were used. The phantom was filled with 10 250 mL of water. A SPECT acquisition was carried through using the standard ^{131}I SPECT protocol, with a 45 s acquisition per projection. Planar images were obtained using the acquisition parameters listed in Table 3.

The SPECT data was reconstructed using the settings presented in Table 6, once again giving three images (*No SC + DEW + TEW*). In each images, circular ROI's (∅ = the true sphere diameter) were defined in all three planes (coronal, sagittal and transaxial), in the slices for which the spheres were centered. The CT image was used as a guide. The mean count rate between the planes was determined for each sphere in each image. Apparent activities were calculated using Eq. (12), and RC's was determined.

Planar images was corrected for scatter, and a geometric mean value matrix was calculated using the posterior and anterior projections. A circular ROI (∅ = the true sphere diameter) was placed over each sphere, and the sphere count rates were determined. Count rates were corrected for attenuation using Eq. (2), assuming attenuation for 11 cm of water, based on the CT image. Once again, apparent activities were calculated with Eq. (12), and the corresponding RC's were determined.

The RC's was plotted as a function of sphere volume V. Using a non-linear least square fit technique, the RC's was fitted to the following function, where c_1 and c_2 denotes the curve fitting parameters.

$$RC = \frac{1}{c_1 \cdot V^{c_2}} \tag{13}$$

3.1.5 Kyoto measurements

As a final step, measurements were preformed using a LK-S Kyoto Liver/Kidney Phantom, see Figure 16. The measurements aimed to evaluate uncertainties in patient-specific quantifications.

The phantom contained a liver compartment of 1800 mL, a 170 mL kidney compartment, as well as two spherical inserts – one with an outer diameter of 3 cm (holding ~10.1 mL) and one with an cm outer diameter of 4 (holding ~25.6 mL). The spheres were filled with 300.0 MBq/L of ^{131}I, 3.0 and 7.8 MBq respectively. The kidney compartment was filled with 145.1 MBq/L, i.e. 24.6 MBq. The inserts were mounted inside the phantom, as seen in Figure 16. Note that the larger sphere is located inside the liver compartment.

Figure 16: *Kyoto phantom*

To test the robustness of the quantifications, three different measurements was performed, to mimic three different patient scenarios. First, the main phantom component was filled with water, while the liver compartment was left empty. This set-up aimed to resemble a patient geometry with a lower level of attenuation and scatter, as in an examination of the chest region. Moving on, the liver compartment was filled with water, to resemble a patient geometry with a higher level of attenuation, but with a cold background. Lastly, the liver compartment was filled with activity, giving a sphere-to-background ratio 15:1, to resemble a patient with a higher level of background activity. The sphere-to-background activity concentration ratio was determined by studying available patient data, choosing the lowest sphere-to-background ratio observed.

The standard planar and SPECT/CT acquisition protocols (see Table 1-3) were used to acquire the images.

The SPECT data was, once again, reconstructed using the settings presented in Table 6. Images were corrected for scatter, giving the sets of images (*No SC* + *DEW* + *TEW*). Activities were determined in the same manner as in the NEMA study;

In the SPECT images, a ROI was defined in each plane (using the CT as a guide) and the mean count rate was calculated. The activity was determined using the calibration factors acquired from the Jaszczak study.

In the planar quantifications, geometric mean value matrices was calculated from the posterior and anterior projections. ROI's were defined using the CT measurements, and count rates were determined. The acquired count rates were corrected for attenuation, once again using measurements from the CT image. In the measurement where the liver compartment contained activity, the background contribution was accounted for using the mean count rate in a ROI close to the structure. Activities were calculated using the calibration factors acquired from the petri dish measurements.

RC's were calculated using the fitted RC curves, see with Eq. (13). For the spheres, the volume was estimated using the diameters of the ROI's defined in the gamma camera images (i.e. using CT measurements). For the kidney, the specified volume of 170 mL was used. Apparent activities were corrected using the RC's, and the quantification errors were determined.

4 Results

4.1 Planar sensitivity and penetration

Figure 17 shows one of the images of the petri dish, acquired at a 10 cm source-to-collimator distance *d*. In Table 7, the planar calibration factors, determined using a small ROI (∅ ≈ 3 cm) centered over the dish, are presented. From Table 7 it appears that DEW correction will induce a more significant reduction in count rate, compared to the TEW correction.

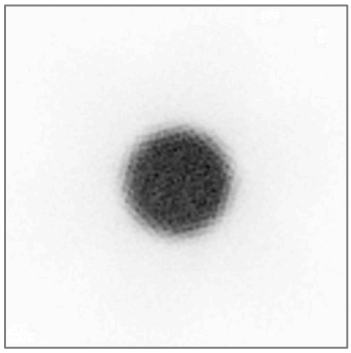

Figure 17: *Planar image of the petri dish, acquired at d = 10 cm.*

Table 7: *Planar calibration factors.*

	No SC	DEW	TEW
K [cps/MBq]	69.7	55.41	60.8

In Figure 18 A), the penetration factor for the non-scatter corrected projections are presented as a function of source-to-collimator distance *d*. It appears that at short source-to-collimator distances, penetration and scatter makes a significant contribution to the recorded count rate. At *d* = 10 cm, the penetration factor was estimated to 14.2%. Figure 18 B) shows the normalized count rate as a function of *d* for the scatter well as non-scatter corrected projections. When applying the scatter corrections, the decrease in count rate was reduced, with the TEW correction giving the smallest variation in count rate over all the distances *d*.

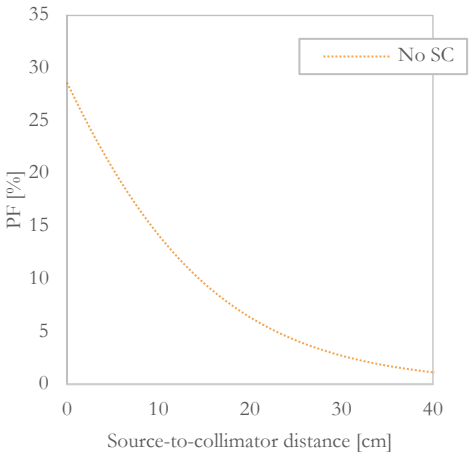

Figure 18 A): *Penetration factor as a function of source-to-collimator distance.*

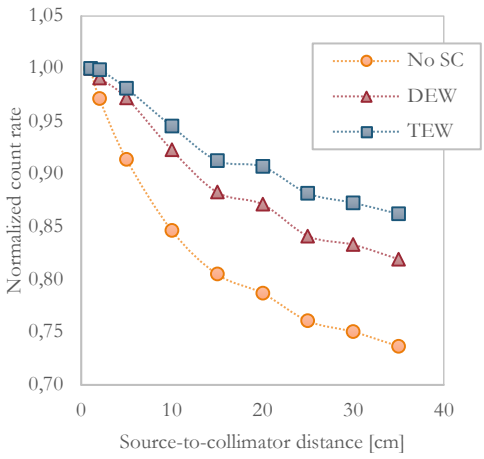

Figure 18 B): *The normalized count rate as a function of source-to-collimator distance.*

4.2 Scatter measurements

Figures 19 A-C) show the acquired projections at thicknesses x = 0, 10 and 20 cm. The projections look similar, however, an increased background signal can be observed as the amount of scattering material is increased. The corresponding DEW and TEW projection matrices, used in the scatter corrections, are shown in Figures 20-21 A-C). When looking at these, the DEW projections gives a noisier impression, compared to the TEW projections. Furthermore, the DEW projections appear to include more background counts, compared to the TEW projections.

In Figure 22 A), the total count rates, corrected for attenuation, are presented as a function of PMMA thickness. As the amount of scattering material increases, the number of counts in non-scatter corrected images appears to increase exponentially. In DEW-corrected images, the total count rate decreases as the PMMA thickness is increased, suggesting that the scatter component is being overestimated in the correction. In TEW-corrected images, the total count rate remains steady throughout all measurements, indicating that the total amount of scattered photons detected is well approximated by the scatter windows chosen. Figure 22 B) shows the count rate within a ROI, centered over the petri dish, as a function of PMMA thickness. For the DEW corrected images, the count rate initially decreases, and later increases as x increases. The TEW corrected count rate appear to remain more or less constant for thicknesses below ~5 cm, however, an increase in count rate can be seen for larger thicknesses.

A) x = 0 cm B) x = 10 cm C) x = 20 cm

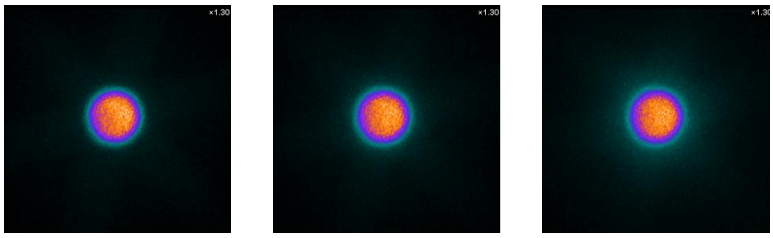

Figure 19 A-C): *Acquired projections at different PMMA thicknesses x.*

A) x = 0 cm B) x = 10 cm C) x = 20 cm

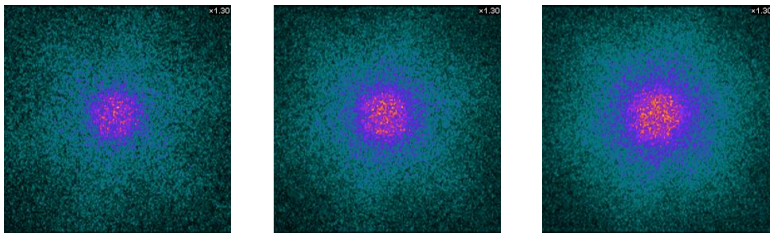

Figure 20 A-C): *DEW matrices acquired at different PMMA thicknesses x.*

A) x = 0 cm B) x = 10 cm C) x = 20 cm

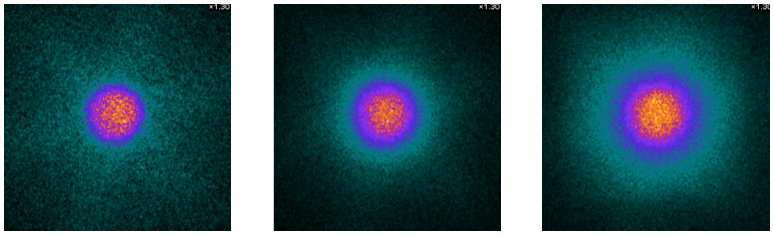

Figure 21 A-C): *TEW matrices acquired at different PMMA thicknesses x.*

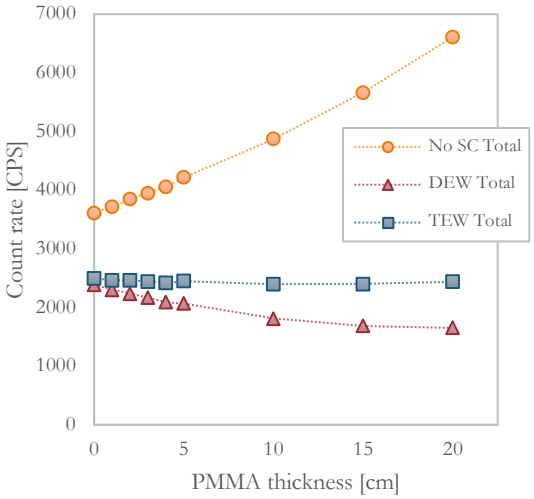

Figure 22 A): *The total recorded count rate as a function of PMMA thickness.*

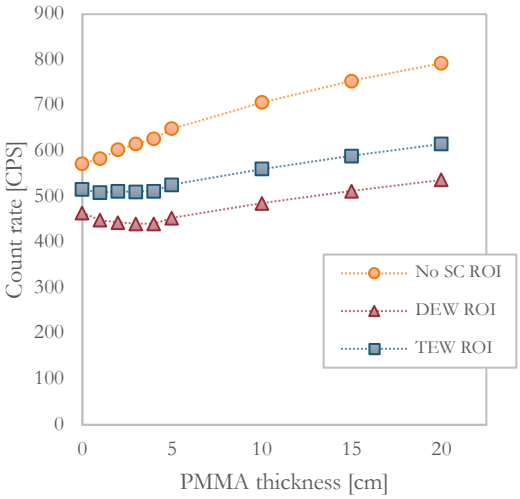

Figure 22 B): *The count rate within a ROI, centered over the dish, as a function of PMMA thickness.*

4.3 System volume sensitivity

Figures 23 A-B) show two reconstructed slices of the Jaszczak phantom. In Table 8, the acquired calibration factors, calculated from a spherical VOI (∅ = 11 cm) defined close to the center of the phantom, are presented. It should be noted that the acquired calibration factors differs from the calibration factors acquired in the planar study, indicating a larger scatter contribution.

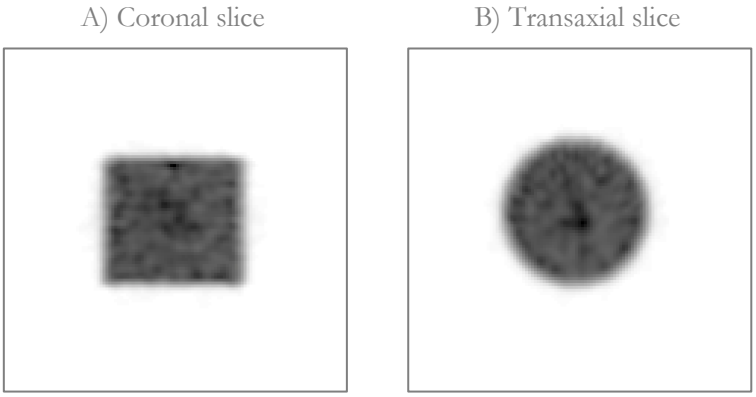

Figure 23 A-B): *Reconstructed (IRACRR) slices of the Jaszczak phantom.*

Table 8: *SPECT calibration factors.*

	No SC	DEW	TEW
K [cps/MBq]	72.6	39.4	47.6

4.4 NEMA measurements

In Figure 24, a planar image of the NEMA phantom is shown. Figures 25 A-C) shows SPECT images of the phantom.

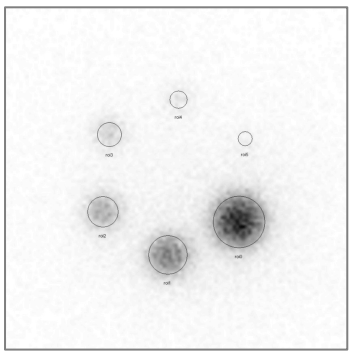

Figure 24: *Planar image of the NEMA phantom.*

A) Transaxial slice B) Coronal slice C) Sagittal slice

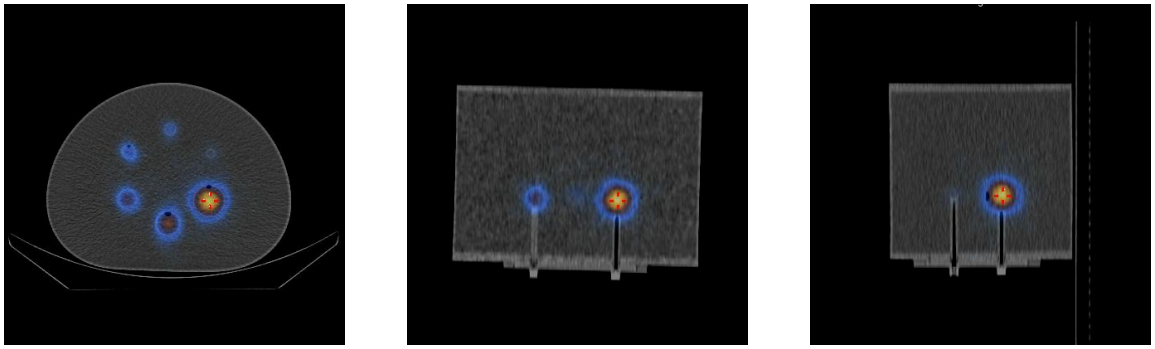

Figure 25 A-C): *SPECT CT images of the NEMA phantom.*

Figure 26 A-C) shows the recovery coefficients for the DEW, TEW and non-SC images in the planar study. In Figure 27 A-C), the corresponding SPECT recovery coefficients are displayed. The curve fitting parameters are presented in Tables 9 and 10.

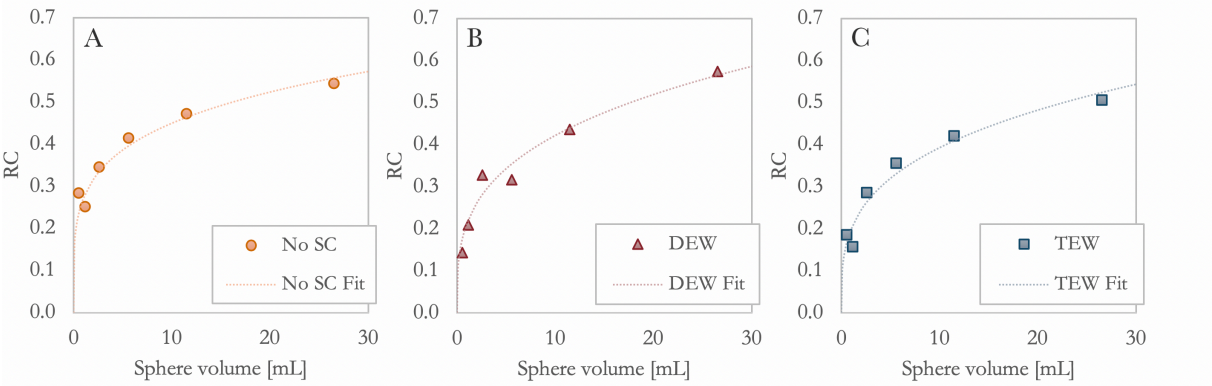

Figure 26 A-C): *Planar recovery.*

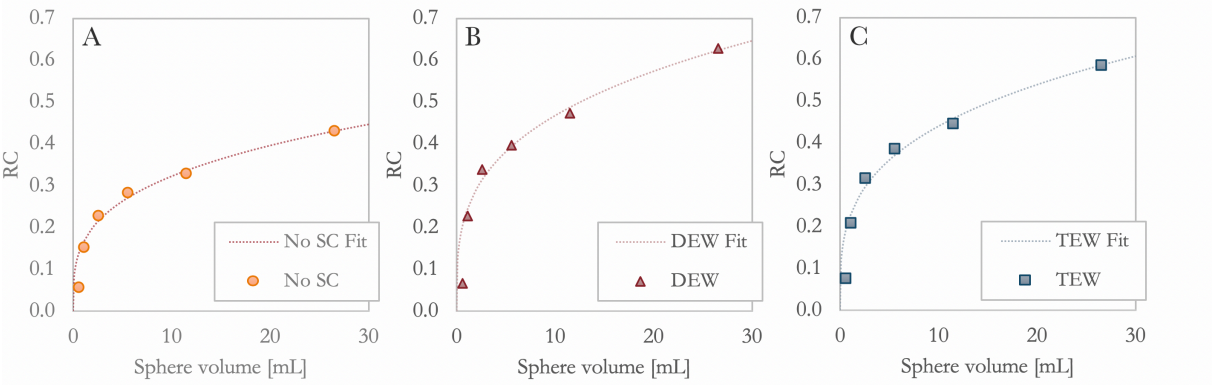

Figure 27 A-C): *SPECT recovery.*

Table 9: *Planar recovery curve fitting parameters.*

	No SC	DEW	TEW
Constant c_1	5.28	5.15	6.40
Constant c_2	0.22	0.28	0.30

Table 10: *SPECT recovery curve fitting parameters.*

	No SC	DEW	TEW
Constant c_1	6.13	4.21	4.46
Constant c_2	0.30	0.29	0.29

4.5 Kyoto measurements

Figure 32 A-C) shows the planar images acquired in the different Kyoto measurements, as well as the ROI's used to quantify the activity. Figures 33 A-C) shows a SPECT image of the phantom from three different views. The recovery coefficients used in the quantifications, calculated using the curve fitting parameters in Tables 9 and 10, are presented in Table 11 and 12.

A) Semi-water filled B) Water-filled C) With background activity

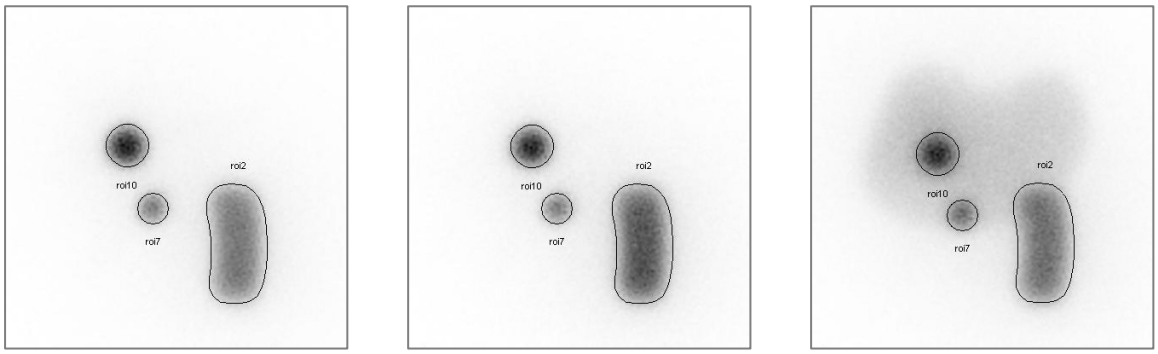

Figure 32 A-C): *Planar images of the Kyoto phantom and he defined ROI's.*

A) Transaxial slice B) Coronal slice C) Sagittal slice

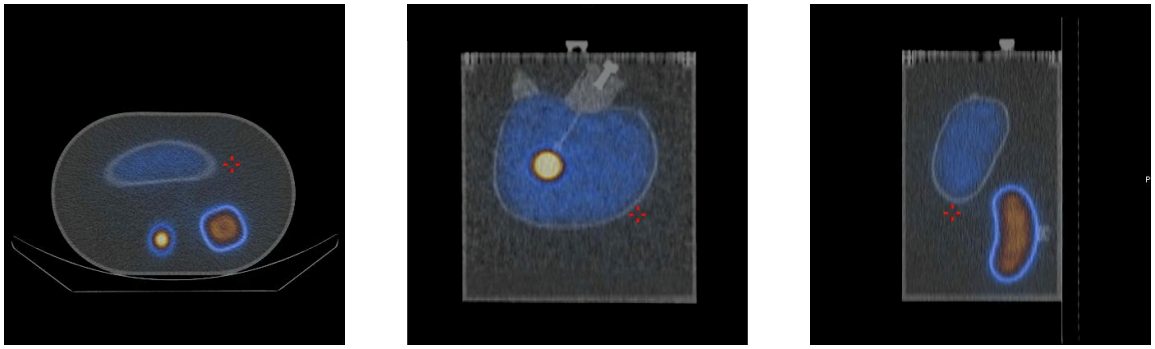

Figure 33 A-C): *SPECT CT images of the Kyoto phantom with background activity.*

Table 11: *Planar recovery coefficients.*

Insert	Volume [mL]	No SC	DEW	TEW
Small sphere	10	0.45	0.42	0.39
Large sphere	26	0.55	0.56	0.52
Kidney	170	0.84	0.99	0.91

Table 12: *SPECT recovery coefficients.*

Insert	Volume [mL]	No SC	DEW	TEW
Small sphere	10	0.32	0.47	0.44
Large sphere	26	0.43	0.62	0.58
Kidney	170	0.72	1.04	0.97

In Figures 34-37 A), the errors attained in the SPECT quantifications, for the three different Kyoto measurements, are presented. Figures 34-37 B) show the corresponding planar quantification errors.

In the SPECT quantifications, similar errors were attained, regardless of the scatter correction. In general, the activity was underestimated. The underestimation was most significant in the measurement where the phantom was semi water-filled. For the spheres, the quantification errors were quite small, see Figures 34-35 A). The highest accuracy was attained for the larger sphere. In the kidney quantifications, see Figure 36 A), the activity was significantly underestimated, indicating that the correction for partial volume effects was insufficient. In non-scatter-corrected images, the background activity was overestimated. However, once the scatter corrections were applied, a small error was attained, see Figure 37 A).

For the planar quantifications, the quantification accuracy was generally poor. The errors for the liver background activity was large, indicating a poor calibration, see Figure 37 B). For the spheres, the activity was overestimated, see Figures 34-35 B), with the overestimation being most significant for the small sphere. Moreover, significant underestimations could once again be observed for the kidney, see Figure 36 B).

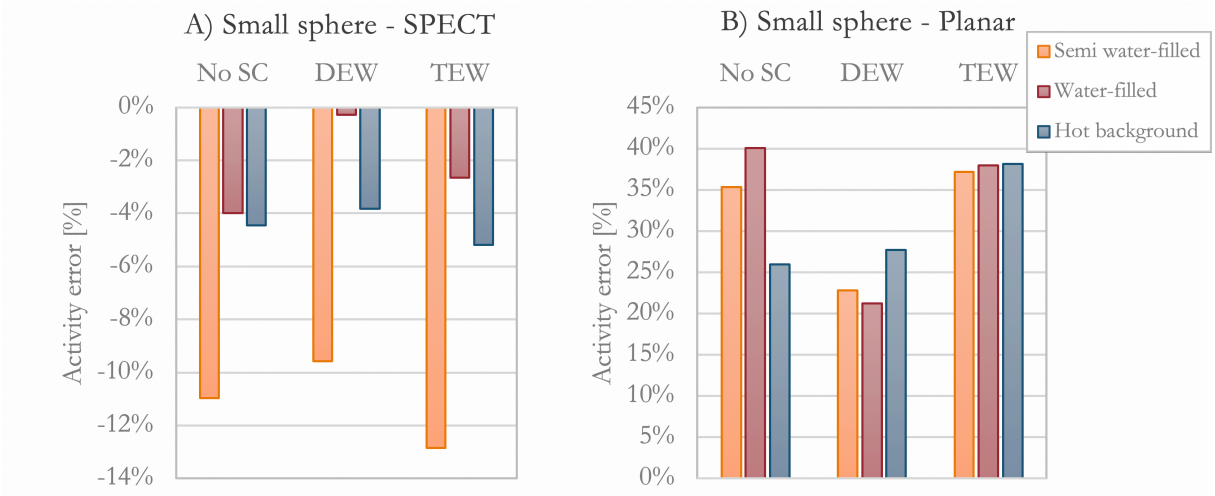

Figure 34 A-B): *Activity quantification error for the 10 mL sphere.*

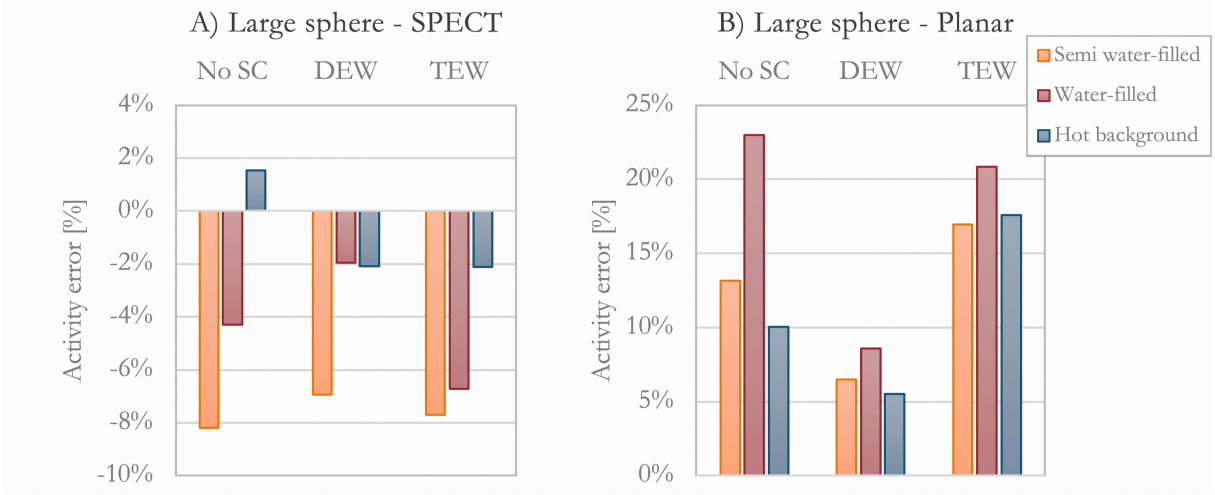

Figure 35 A-B): *Activity quantification error for the 26 mL sphere.*

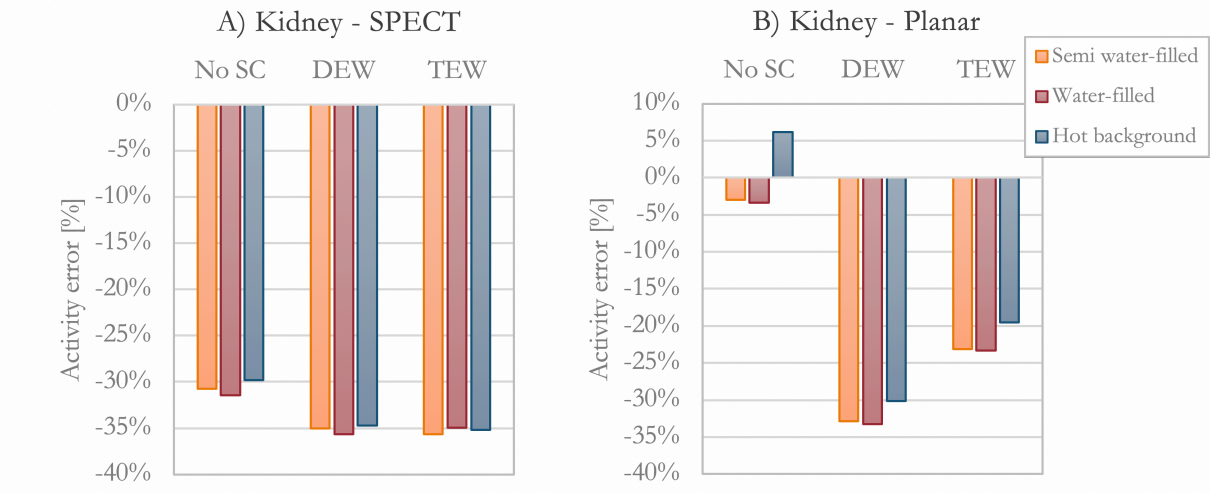

Figure 36 A-B): *Activity quantification error for the 170 mL kidney.*

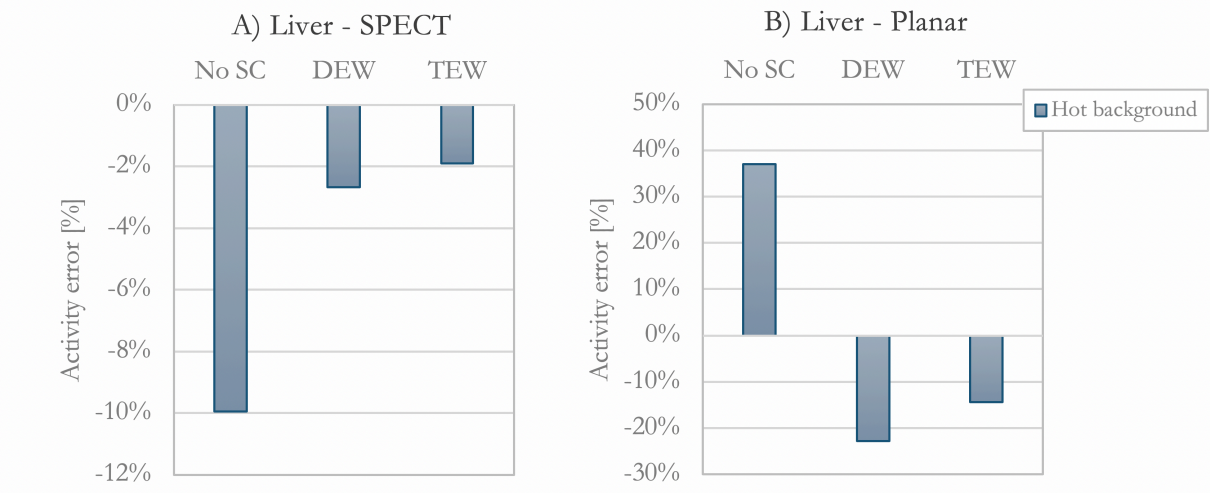

Figure 37 A-B): *Quantification error for the liver background activity.*

5 Discussion

5.1 Planar measurements of penetration and scatter

In the penetration study, a very distinct exponential decline was observed when studying the recorded count rate as a function of source-to-collimator distance *d*, see Figure 18 B). The observed trend clearly highlights one important issue in imaging and quantifications with ^{131}I, as it points towards a high level of degradation due to scatter and penetration. More specifically, the fraction of penetration was estimated to 15% at a 10 cm source-to-collimator distance, see Figure 18 A). In addition, the penetration study aimed to examine how the spatially varying response would be affected by applying a scatter correction. When looking at the scatter corrected count rates, see Figure 18 B), it is apparent that the relative variation in response was reduced once the corrections were applied. It can also be concluded that the TEW correction is more efficient at compensating for the variation in response, compared to the DEW correction. In other words, the results from the penetration study suggest that a TEW correction is most effective when compensating for variations in detection efficiency due to scatter and penetration.

In the study of scatter, the total count rate in the TEW-corrected images appeared to remain constant as the amount of scattering material was increased, while a reduction in count rate was observed in the DEW-corrected images, see Figure 22 A). The reason for this becomes apparent when studying the recorded gamma spectra, see Appendix I. As the PMMA thickness is increased, the number of counts recorded in the lower energy window will increase significantly. However, the increase in counts for energy channels situated above the photopeak is not as substantial. The large increase in counts at energies below the photopeak can be attributed to the more effective attenuation of 364 keV photons, in comparison to higher-energy emissions. In addition, the relative loss of energy is smaller for the 364 keV photons, allowing more photons to register within the adjacent lower energy window. In conclusion, scattered 364 keV photons will make a large contribution in the lower energy window, resulting in an overestimation of the total scatter component in the DEW-correction, while the TEW correction provides a good approximation.

Nevertheless, the total count rate is not a perfect indicator of how well the scatter correction works, as it does not take into consideration the spatial distribution of the counts. The scatter component will vary from pixel-to-pixel, as each pixel will corresponds to its own unique energy spectrum. Hence, a pixel-wise subtraction will impact the count rate differently throughout the acquired image. When studying the count rate within a small ROI centered over the petri dish, see Figure 22 B), a different trend can be observed compared to for the total recorded count rate. In the DEW-corrected images, the count rate initially decreases, and later increases as more scattering material is added. The TEW-corrected images displays a similar trend, however, the count rate appears more stable for small amounts of scattering material. This is an important observation, as it highlights the fact that the scatter component can be both under- and overestimated, depending on the level of attenuation. The observed trend can once again be understood by studying the acquired gamma spectra, see Appendix I, and in particular by looking at the contribution from the 283 keV peak. For small amounts of scattering material, the relative contribution from the 283 keV peak at energies below the photopeak is quite large. However, as the amount of scattering material increases, the contribution from scattered 364 keV photons become more prominent. Hence, the contribution from 283 keV photons results in an overestimation of the scatter component at small scattering thicknesses. As the window for the DEW correction practically covers the entire 283 keV peak, the effect is most noticeable in this correction. Once again, the results point towards the TEW correction being a more suitable option. In addition, the observations made highlight the importance of regarding the spatial distribution of counts in the correction matrices when evaluating the corrections.

The distribution of the scattered counts in the DEW and TEW correction matrices can be seen in Figures 20-21 A-C). From these images, it appears that the DEW correction tend to remove counts from all throughout the image, while the scattered counts in the TEW correction seem to follow the outline of the source. Also, the DEW projections appears noisier, compared to the TEW projections. This is another important observation, as the noise properties of the correction may ultimately affect the quantification accuracy – especially when using a reconstruction algorithm with noise enhancing qualities.

In conclusion, the results suggests that the scatter and penetration component is best approximated by a TEW correction. However, it should be noted that these observations apply to planar measurements of a planar source. In a three-dimensional source geometry, photons would originate from different depths within the examined object, resulting in a variation in count rate due to both a variation in source-to-collimator distances, as well as to different levels of attenuation. It is difficult to predict how these effects would play out in a more complex geometry, and how that in turn would affect the quantification accuracy. Still, the smaller variation in count rate observed when using the TEW correction is a clear indicator that the this method is a more reliable option, as is therefore to be preferred over a DEW correction. Nevertheless, the energy window settings would need further optimization, and the correction method should be tested using more complex source geometries.

5.2 Kyoto quantifications

When applying the quantification method to the images of the Kyoto phantom, the scatter correction appears to have little impact on the accuracy of the quantifications. Instead, the accuracy seem to depend mostly on the source geometry, as well as the attenuation properties of the phantom. This implies that the scatter correction alone cannot compensate for the variation in count rate due to the variation in geometry, which in turn highlights the importance of an adequate calibration and a robust partial volume correction.

5.2.1 Calibration and quantification accuracy

The adequacy of the calibration can be evaluated by studying the errors acquired in the quantifications of liver background activity. For the SPECT images, see Figure 37 A), errors were quite small. With no scatter correction, the background activity was underestimated by 10%. This is not very surprising, as the liver compartment contains a much smaller volume of activity, compared to the Jaszczak phantom (1.8 and 6.8 L respectively). Hence, it is reasonable that the fraction of scatter would be lower in the Kyoto study compared to in the calibration study, explaining the observed error. However, once the scatter corrections were applied, errors were significantly reduced for both DEW and TEW corrected images (to ~2%). It thus appears that the reduced scatted contribution that comes with a reduction in volume of activity is well accounted for by the scatter correction, and that the calibration factors acquired in the Jaszczak study (see Table 7) works well when quantifying background activity.

In the Kyoto SPECT quantifications, see Figures 34-37 A), the activities were generally underestimated. For the spheres, the largest underestimations were attained in the measurement in which the liver compartment was left empty. This is understandable, as the amount of scattering material was quite considerably reduced compared to in the calibration study, hence reducing the number of scattered counts recorded. A smaller error was attained once the phantom was completely water-filled, and similar uncertainties were attained when background activity was added. This is an important observation, as it indicates that the scatter correction is not very efficient at compensating for variations in the total amount of scattering material. Hence, it appears that the total amount of scattering material is much more crucial to the accuracy of the quantification, rather than the total volume of activity. This underlines the importance of an appropriate calibration, in which the attenuation properties of the examined object is well simulated.

It should however be noted for the kidney, similar quantification errors were obtained regardless of whether the phantom was completely water-filled or not. In other words, it appears that the deviation between measurements is reduced with increasing quantification volume, indicating that smaller structures are much more susceptible to variations in geometry and in the level of attenuation.

It should also be noted that the sphere-to-background activity concentration ratio used in the experiment was quite high (15:1), making the count contribution from spill-in effects small. If a higher background concertation had been used, spill-in effects would likely have become more prominent, potentially resulting in an overestimation of the quantified activity. However, when studying patient data, activity concentration ratios above 15:1 were rarely observed, making such effects unlikely. Moreover, a high background activity, or a high activity over all, may induce deadtime, which could affect the quantification accuracy. Hence, it would be appropriate to assess to total number of counts recorded prior to preforming patient quantifications, and potentially adjust the calibration factor, if deemed necessary.

In the planar quantifications, see Figures 34-37 B), errors were generally much larger compared to in the SPECT quantifications. This can be attributed to many different factors. First of all, the calibration factors used (see Table 6) do not resemble the scattering properties of the Kyoto phantom. The inadequate calibration manifests clearly in the background activity quantifications. In the non-scatter corrected image, see Figure 37 B), the background activity was overestimated by 40%, indicating a much higher level of scatter in the Kyoto study, compared to in the calibration study. Accordingly, the activity was underestimated in scatter-corrected images, due to the increased number of counts recorded in the scatter windows, as compared to the calibration measurement. The large error is not very surprising, as the planar calibration factors were determined through an in-air acquisition of a planar source. To improve the accuracy, the calibration factor would have to be determined using a source geometry with a higher level of attenuation and scatter.

5.2.2 Quantification of spherical structures

In the SPECT quantifications of the sphere activities, errors were generally quite small, see Figures 34-35 A). As previously established, the largest errors were attained for the semi water-filled Kyoto phantom, in the order of -11% and -7% for the small and large sphere respectively. Once the phantom was filled, the accuracy was improved, giving errors in the order of -4% for the smaller sphere and -2% for the larger sphere. The small errors suggests that the calibration was adequate, and that partial volume effects were well accounted for. However, larger errors were generally attained for the smaller sphere, see Figure 34 A). This can be attributed to many factors, the first being the size. The smaller sphere is only 2.6 cm in diameter, which equivales to approximately 6 pixels. As the structure is small in relation to the resolution, it will be more susceptible to the various sources of error. Most importantly, the effects of partial volume and spill-over will be more prevalent, as a larger fraction of pixels are adjacent to the background. Consequently, the preciseness of the source delineation, and the partial volume correction, will be more crucial to the accuracy. However, the errors may also have been affected by the geometry of the phantom. The smaller located more peripherally, compared to the larger sphere. Hence, the contribution from scatter and penetration may differ. It is difficult to foresee how this may have influenced the result. However, it is important to keep in mind that a small volume is generally associated with a larger error.

The scatter correction appeared to have little impact on the accuracy of the results, which once again points to the importance of the calibration and partial volume correction. In non-scatter corrected images, the partial volume correction will more or less act as a calibration, as it accounts for the variations in scatter and penetration. Consequently, when looking at the results it appears that accurate, non-scatter corrected quantifications are feasible. This is an important observation, as scattering data is lacking for the vast majority of patient images already acquired at SUS. However, if quantifications are performed on non-

scatter corrected images, it is very much crucial that the scatter is component is well approximated in the calibration and/or partial volume study. If not, major errors can may be induced. A perfect calibration and partial volume correction is of course very hard to attain. Hence, quantifications without scatter correction should be done with caution.

As previously discussed, the planar quantifications, see Figures 34-37 B), generated large errors in comparison to the SPECT quantifications. This is partially due to the poor calibration. However, there are additional sources of error associated with planar quantifications, which are likely to have influenced the result. Most importantly, the accuracy of the planar quantifications is very much dependent on the preciseness of the attenuation correction. In this study, the attenuation properties of the phantom was known thanks to the acquired CT scan. However, in a clinical scenario, this information might not be available. In such cases, the correction for attenuation could potentially introduce very significant errors. There are also additional sources of error that may have affected errors, such as the reduced total acquisition time and correction for superimposed background activity.

5.2.3 Partial volume and object shape effects

Spill-over effects can be a major source of error in ^{131}I quantifications, as the spatial resolution is comparatively poor. When analyzing the results, it is apparent that the partial volume correction is crucial to the accuracy of the result. This becomes especially clear when looking at the quantifications of the kidney activity, see Figures 36 A-B). In the SPECT quantifications, the activity was underestimated by 35% in scatter corrected images, and 30% in non-scatter corrected images. However, the deviation between different measurements was small (<2%). This indicates that for a larger volume, the quantification accuracy is less dependent on the patient geometry, and more on the calibration and the correction for partial volume effects.

The large error is partially due to the fact that no recovery coefficient was determined for volumes as large as the kidney (170 mL), as the study of partial volume effects only included volumes from 0.5 to 26.5 mL, see Figures 26-27 A-C). Although the fitted curve seem to approximate the recovery well within the examined interval, the true convergence behavior of the recovery is still unknown. Hence, the results relies heavily on the accuracy of the extrapolation of the fitted curve, see Tables 10-11. For the kidney, the extrapolated recovery coefficients were close to one. It is however apparent when looking at the results that not all of the activity was recovered, see Figures 36 A-B).

However, the quantification error in the kidney study is not only due to the size of the structure, but also the shape. The kidney insert is more cylindrical in shape, rather than spherical. In a study by Dewaraja YK. et. al.[26] the influence of object shape effects in ^{131}I quantifications was assessed through Monte Carlo simulations of various source geometries. In the study, they conclude that spill-over effects are more significant for non-spherical structures than for spherical structures. They also state that a lower number of counts was recovered for cylindrical shaped structures, compared to for spherical structures. The inaccuracy could be improved by applying a sphere-based partial volume correction, however, large errors were attained in some cases. For a 50 mL cylinder in a cold background, a -39% error was attained. For a 200 mL irregular structure, the activity was underestimated by 35%. These observations align well with the results of this study, indicating that shape of the kidney is likely to have impacted the result. The impact of a varying object shape is a very important observation, as tumors in patients are seldom spherical. Hence, the shape of a lesion could have considerable effect on the quantification accuracy.

[26] Dewaraja YK, Ljungberg M, Koral FK. Monte Carlo evaluation of object shape effects in iodine-131 SPET tumor activity quantification. Eur J Nucl Med. 2001;28:900–906.

In summary, the large errors attained in the kidney quantifications reveal the importance of an robust partial volume correction that considers both the size and shape of a lesion, and that in order for highly accurate patient quantifications to be attained, these effects need further assessment.

It should be noted that the calibration factor chosen for the study will determine the influence of the partial volume correction. In this study, the SPECT calibration factors were attained using a spherical VOI in uniform activity, meaning that no partial volume effects were present. Although small errors was attained when quantifying background activity, only a small fraction of activity could be recovered in the quantifications, due to the very significant partial volume degradation. As seen in the sphere quantifications, a precise partial volume correction will recover the lost activity. However, the chosen calibration factor inevitably makes the preciseness of the partial volume correction very important to the final accuracy. If the calibration factor would have been determined using an activity filled insert in water, more activity would have been recovered in the quantifications. This would likely have improved the results of the kidney quantifications. In addition, alternative methods of target delineation could improve the accuracy, if no adequate partial volume is in place.

5.4 Conclusions

Planar studies of scatter and penetration showed that a TEW correction is more effective than a DEW correction. In quantifications however, the scatter correction had little impact on the accuracy of the result. Instead, the accuracy largely depended on the adequacy of the calibration as well as the partial volume correction. It appears that non-scatter corrected quantifications are feasible, however, it would require a highly accurate calibration, which would be difficult to attain in a clinical setting. A varying patient geometry could potentially induce significant errors, even for scatter-corrected images, if the calibration is not accurate.

Small structures and objects of with a non-spherical shape are generally associated with larger errors. Applying sphere-based recovery coefficient to an irregularly shaped structure may potentially induce significant quantification errors. In order for highly accurate patient quantifications to be attained, the impact of partial volume effects for large and non-spherical structure would need assessment.

With the method, accurate SPECT quantifications are feasible. The largest potential source of error is object shape effects and a varying patient geometry. Planar quantifications are generally associated with larger errors, and accurate planar quantifications would be difficult to achieve clinically, due to many potential sources of error.

5.5 Future prospects

Most importantly, the impact of partial effects on large an non-spherical need assessment. Furthermore, the energy window settings for the TEW correction needs to be optimized, and evaluated with regards to more complex geometries. Also, alternative methods of target delineation should be examined. The calibration of the system sensitivity should be further evaluated, and alternative calibration methods tested. Moreover, the sources of error associated with patient imaging, such as variations in patient geometry and ^{131}I uptake, should be examined more thoroughly. In addition, the effects of different reconstruction settings and an increased number of iterations should be evaluated. Lastly, in order for dosimetry to performed, methods of mass determination and determination of effective half-life would have to be examined.

6 References

[1] NORDCAN. Cancer Statistics Fact Sheet – The Thyroid Gland. Association of the Nordic Cancer Registries; 2019.

[2] Swedish Cancer Society. Cancerfondsrapporten 2018. Stockholm: Swedish Cancer Society; 2018.

[3] Winslow T. Anatomy of the Thyroid and Parathyroid Glands [Illustration]. 2012. [cited 2019-07-05] Available from: *https://www.teresewinslow.com/head/nmpuvgu8p79zjo65f2wx0i6g7b6du7*

[4] Nussey S, Whitehead S. Endocrinology: An Integrated Approach. Oxford: BIOS Scientific Publishers; 2001. Chapter 3, The thyroid gland. Available from: *https://www.ncbi.nlm.nih.gov/books/NBK28/*

[5] Swedish Cancer Society. Sköldkörtelcancer [Internet]. Stockholm: Swedish Cancer Society; 2018 [updated 2018-11-26; cited 2019-04-18]. Available from: *https://www.cancerfonden.se/om-cancer/skoldkortelcancer*

[6] Haugen BR, Alexander EK, Bible KC, Doherty GM, Mandel SJ, Nikiforov YE et al. 2015 American Thyroid Association Management Guidelines for Adult Patients with Thyroid Nodules and Differentiated Thyroid Cancer: The American Thyroid Association Guidelines Task Force on Thyroid Nodules and Differentiated Thyroid Cancer. Thyroid. 2016;26(1):1–133.

[7] Laboratoire National Nehri Becquerel. Atomic and Nuclear data, I-131 table. [Internet] Gif-sur-Yvette Cedex, France: Laboratoire National Nehri Becquerel; 2001 - . [updated 2014-01-20; cited 2019-04-20]. Available from: *http://www.lnhb.fr/nuclides/I-131_tables.pdf*

[8] NIST. ESTAR: Stopping Power and Range Tables for Electrons. [Internet] Gaithersburg, USA: National Institute of Standards and Technology; 1998 - . [updated July 2017; cited 2019-07-05]. Available from: *https://physics.nist.gov/cgi-bin/Star/e_table.pl*

[9] NIST. X-ray Mass Attenuation Coefficents. [Internet] Gaithersburg, USA: National Institute of Standards and Technology; 1998 - . [updated July 2004; cited 2019-07-05]. Available from: *https://physics.nist.gov/PhysRefData/XrayMassCoef/ComTab/water.html*

[10] Knoll GF. Radiation Detection and Measurement. 4th edition. USA: Wiley; 2010.

[11] Khalil MM. Basic Sciences of Nuclear Medicine. Berlin Heidelberg: Springer-Verlag; 2011. 10, Elements of Gamma Camera and SPECT Systems. p. 155-78.

[12] Bruyant PP. Analytic and Iterative Reconstruction Algorithms in SPECT. J Nucl Med. 2002 Oct;43(10):1343-58.

[13] Ljungberg M, Pretorius PH. SPECT/CT: an update on technological developments and clinical applications. Br J Radiol. 2018 Jan; 91(1081): 20160402.

[14] Sorenson JA, Phelps ME. Physics in Nuclear Medicine. 2nd ed. United States; Elsevier; 1987. 16; The Anger Camera: Performance Characteristics. p. 331-45.

[15] NEMA. Performance Measurements of Gamma Cameras. Rosslyn: National Electrical Manufacturers Association; 2007.

[16] IAEA. Nuclear Medicine Physics: A Handbook for Teachers and Students. Vienna: International Atomic Energy Agency; 2014.

[17] Ritt P, Vija H, Hornegger J, Kuwert T. Absolute Quantifications in SPECT. Eur J Nucl Med Mol Imaging. 2011 May;38 Suppl 1:S69-77.

[18] Ljungberg M. Quantitative SPECT Imaging. In: Khalil MM, editor. Basic Sciences of Nuclear Medicine. Berlin Heidelberg: Springer-Verlag; 2011. p. 285-309.

[19] Jaszczak RJ, Greer KL, Floyd CE Jr, Harris CC, Coleman RE. Improved SPECT quantification using compensation for scattered photons. J Nucl Med. 1984 Aug;25(8):893-900.

[20] Ogawa K, Harata Y, Ichihara T, Kubo A, Hashimoto S. A practical method for position-dependent Compton-scatter correction in single photon emission CT. IEEE Trans Med Imaging. 1991;10(3):408-12.

[21] Gunter DL. Collimator Design for Nuclear Medicine. In: Wernich MN, Aarsvold JN, editors. Emission Tomography: The Fundamentals of PET and SPECT. San Diego, California, USA: Elsevier; 2004. p.160-61.

[22] IAEA. Quantitative Nuclear Medicine Imaging: Concepts, Requirements and Methods. Vienna: International Atomic Energy Agency; 2014. IAEA Human Health Series, ISSN 2074; no. 9.

[23] Soret M, Bacharach SL, Buvat I. Partial-Volume Effect in PET Tumor Imaging. J Nucl Med 2007; 48:932–945.

[24] Dewaraja YK, Frey EC, Sgouros G, Brill AB, Roberson P, Zanzonico PB, et al. MIRD Pamphlet No. 23: Quantitative SPECT for Patient-Specific 3-Dimensional Dosimetry in Internal Radionuclide Therapy. J Nucl Med 2012; 53:1310-1325.

[25] Dewaraja YK, Ljungberg M, Green AJ, Zanzonico PB, Frey EC, SNMMI MIRD Committee, et al. MIRD Pamphlet No. 24: Guidelines for Quantitative 131I SPECT in Dosimetry Applications. J Nucl Med. 2013;54:2182-2188.

[26] Dewaraja YK, Ljungberg M, Koral FK. Monte Carlo evaluation of object shape effects in iodine-131 SPET tumor activity quantification. Eur J Nucl Med. 2001;28:900–906.

7 Appendix

7.1 Gamma spectrum

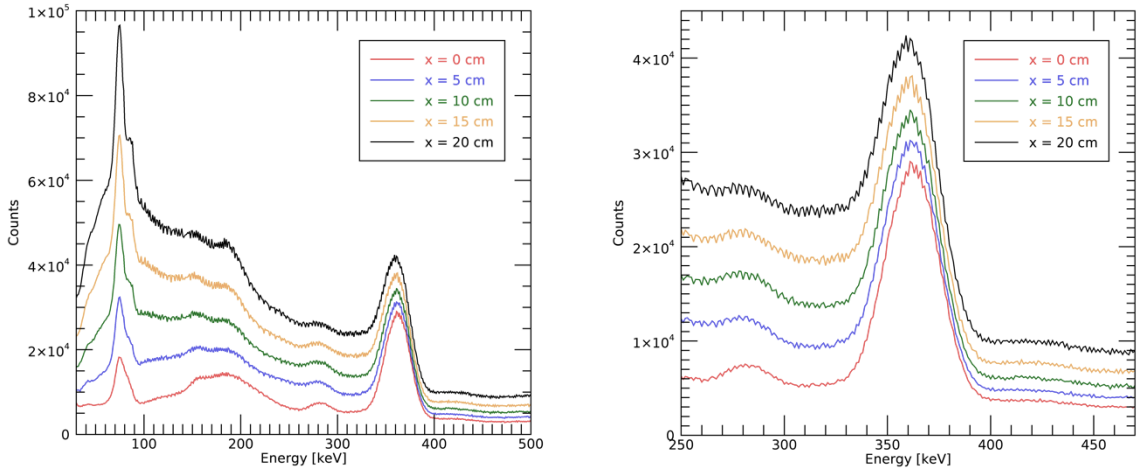

Figure 38: *Images of the gamma spectra acquired with PMMA thicknesses 0, 5, 10, 15 and 20 cm.*

LUND
UNIVERSITY